

Detection of significant climatic precession variability in early Pleistocene glacial cycles

Parker R. Liautaud^{a,*}, David A. Hodell^b, Peter J. Huybers^a

^a*Department of Earth and Planetary Sciences, Harvard University, Cambridge, MA 02138, United States*

^b*Godwin Laboratory for Palaeoclimate Research, Department of Earth Sciences, University of Cambridge, Cambridge CB2 3EQ, United Kingdom*

Abstract

Despite having a large influence on summer insolation, climatic precession is thought to account for little variance in early Pleistocene proxies of ice volume and deep-water temperature. Various mechanisms have been suggested to account for the dearth of precession variability, including meridional insolation gradients, interhemispheric cancellation of ice-volume changes, and antiphasing between the duration and intensity of summer insolation. We employ a method termed Empirical Nonlinear Orbital Fitting (ENOF) to estimate the amplitudes of obliquity and precession forcing in early Pleistocene proxies and their respective leads or lags relative to the timing of orbital variations. Analysis of a high-resolution North Atlantic benthic $\delta^{18}\text{O}$ record, comprising data from IODP sites U1308 and U1313, indicates a significantly larger precession contribution than previously recognized, with an average precession-to-obliquity amplitude ratio of 0.51 (0.30-0.76 95% confidence interval) in the rate-of-change of $\delta^{18}\text{O}$ between 3 and 1 Ma. Averaged when eccentricity exceeds 0.05, this ratio rises to an average of 1.18 (0.84-1.53). Additional support for precession's importance in the early Pleistocene comes from its estimated amplitude covarying with eccentricity, analyses of other benthic $\delta^{18}\text{O}$ records yielding similar orbital amplitude ratios, and use of an orbitally-independent timescale also showing significant precession. Precession in phase with Northern Hemisphere summer intensity steadily intensifies throughout the Pleistocene, in agreement with its more common identification during the late Pleistocene. A Northern Hemisphere ice sheet and energy balance model run over the early Pleistocene predicts orbital amplitudes consistent with observations when a cooling commensurate with North Atlantic sea surface temperatures is imposed. These results provide strong evidence that glaciation is influenced by climatic precession during the late Pliocene and early Pleistocene, and are consistent with hypotheses that glaciation is controlled by Northern Hemisphere summer insolation.

Keywords: Milankovitch, Pleistocene, precession, glacial cycle, spectral analysis, orbital forcing.

*Corresponding author

Email address: parker_liautaud@g.harvard.edu (Parker R. Liautaud)

1. Introduction

Adhémar (1842), Croll (1864), and Murphy (1869) each argued in turn that ice ages are initiated by changes in the duration and intensity of the seasons. Adhémar (1842) suggested that long winters favor the growth of ice sheets, while Croll (1864) proposed that cold winters are the most favorable, and Murphy (1869) that cool summers, unable to melt the previous winter's snowfall, are responsible. All three yet agreed that "only one hemisphere, the northern or the southern, has a glacial climate at the same time" (Murphy, 1869), citing the important influence of climatic precession on the duration and intensity of seasons. Climatic precession, whose influence is anti-phased between the hemispheres, arises from the precession of Earth's rotational axis, at a period of 25.7 ky, which when combined with apsidal precession gives an overall period that ranges between 18 and 24 ky. Its effect on climate is modulated by the orbital eccentricity.

Milankovitch (1941) rejected the view that hemispheres were alternately glaciated, arguing instead that a Northern Hemisphere glacial advance has global consequences by changing the planetary albedo. Using more accurate calculations of variations in obliquity – which produce in-phase changes in insolation across both hemispheres – than had been available to his predecessors, Milankovitch predicted the timing of ice ages from variations in the summer caloric half-year, or the insolation averaged over the half of the year that maximizes the resulting value, on which precession and obliquity have nearly equal influence. A number of studies have confirmed Milankovitch's hypothesis in the late Pleistocene; for example, sea-level highstands demonstrate variability consistent with Milankovitch's hypothesized precession phase (e.g. Broecker et al., 1968), and other climate proxies feature obliquity and precession amplitudes consistent with Milankovitch's hypothesized forcing (Hays et al., 1976; Imbrie et al., 1992). But whether Milankovitch's theory, or indeed any theory calling upon precession as causing fluctuations in ice volume, also holds for the early Pleistocene and late Pliocene is much less clear, because $\delta^{18}\text{O}$ measured in benthic foraminifera has been interpreted to vary almost exclusively at the obliquity period of 41 ky during this earlier epoch, with apparently

negligible variance at precession periods (Ruddiman et al., 1986).

Several explanations have been proposed for the 41-ky ice ages. Raymo and Nisancioglu (2003) proposed that the meridional insolation gradient, which varies primarily at the obliquity period, could drive heat and moisture fluxes that would control the ice sheet mass balance, but this would require that the ice sheet be equally sensitive to lower-latitude and local insolation. Loutre et al. (2004) asked whether the mean annual insolation, which features no precession variance, could drive long-term climate variability, and also proposed a role for the meridional insolation gradient in driving poleward moisture transport. Huybers (2006), modifying the caloric half-year model of Milankovitch (1941), argued that the influence of precession-induced changes in insolation intensity were canceled by an opposing change in summer duration. The degree of precession cancellation would depend on several factors, including the average global temperature and the meridional extent and thickness of the ice sheet (Huybers and Tziperman, 2008).

Contrasting with explanations excluding precession from the forcing, Raymo et al. (2006), extending the model of Murphy (1869), argued that local summer intensity does control ablation, but its anti-phased response between the hemispheres results in a cancellation of the precession signal in $\delta^{18}\text{O}$ records. This would require that the Southern Hemisphere contribution to changes in $\delta^{18}\text{O}$ nearly balance and be well-mixed with that of the Northern Hemisphere despite the Northern ice sheets lying at comparatively low latitude (Alley, 1991), with an ablation margin exposed to insolation more strongly influenced by precession. The foregoing mechanisms are not mutually exclusive, and Tabor et al. (2015) suggested that a combination of factors including eccentricity modulation of the precession amplitude and obliquity’s longer period relative to precession increase the obliquity response relative to precession.

Evidence for the presence of precession in early Pleistocene glacial cycles is not entirely absent. An analysis of globally-distributed benthic $\delta^{18}\text{O}$ records suggested that the amplitude of climate variability at precession frequencies follows the long-term amplitude modulations of climatic precession

throughout the Plio-Pleistocene (Lisiecki and Raymo, 2007), and precession has long been identified
 in early Pleistocene planktonic $\delta^{18}\text{O}$ records for use in the construction of age models (Shackleton
 et al., 1990). A further important finding is that not all early Pleistocene glacial cycles are symmetric
 (Ashkenazy and Tziperman, 2004; Lisiecki and Raymo, 2007), with rates of deglaciation appearing
 to exceed those of glaciation in some cycles. This asymmetry suggests a nonlinear response to or-
 bital forcing and is qualitatively consistent with late Pleistocene climate variability, albeit of smaller
 magnitude (Huybers, 2007). Because precession does not change the net annual insolation, only re-
 distributing it across seasons (Rubincam, 1994), its appearance in climate proxies must result from a
 nonlinearity in the climate response (Rubincam, 2004) or how it is recorded (Huybers and Wunsch,
 2003). Precession might therefore be expected to accompany apparently nonlinear variability during
 the early Pleistocene, just as it does similar asymmetric variability in the late Pleistocene. These
 factors motivate our revisiting the substantiality of precession forcing in early Pleistocene glacial
 cycles.

2. Data

We evaluate a composite, high-resolution benthic $\delta^{18}\text{O}$ record from the North Atlantic ocean span-
 ning 3 Ma to the present, referred to as L2H19 (Figure 3a). L2H19 comprises data from IODP Site
 U1313 between 3 Ma and 2.42 Ma and from Site U1308 thereafter. The combined record features an
 average temporal resolution of 0.3 ky from 1.62 Ma to present, 1.3 ky from 2.42 to 1.62 Ma, and 2.1
 ky from 3.0 to 2.42 Ma. L2H19 complements analysis of an average over many records, or a stack,
 because of its high resolution and because small differences in the age models of individual records
 may smooth $\delta^{18}\text{O}$ variability when records are averaged (Huybers and Wunsch, 2004).

The choice to patch U1313 between 3 Ma and 2.42 Ma was made for purposes of having a complete
 and undistorted record. Although U1308 extends to beyond 3 Ma, it contains a hiatus between 2.6

83 and 2.65 Ma that skips Marine Isotope Stages (MIS) G1 and G2, and low sedimentation rates or a
84 short hiatus distorts MIS 97 and 98 (Hodell and Channell, 2016). U1313 provides a more complete
85 record in the late Pliocene (Bolton et al., 2010), and its benthic $\delta^{18}\text{O}$ values closely align with those
86 of U1308 where they overlap except with minor amplitude mismatches from 2.7 to 2.9 Ma. Both
87 records are drilled at similar water depths, with U1313 at 3426m and U1308 at 3882m, and the
88 shipboard spliced composite sections were checked for completeness. U1313 and U1308 are spliced
89 together by taking mean values across an overlap of 10 ky at 2.42 Ma (Figure A1).

90 Five other benthic $\delta^{18}\text{O}$ records that extend into the early Pleistocene are also evaluated, and their
91 characteristics are listed with those of L2H19 in Table 1. Two records, one from DSDP Site 607
92 and the second from ODP Sites 980 and 981, are from the North Atlantic. The three other records,
93 from ODP Sites 677, 846, and 849, are from the equatorial Eastern Pacific.

94 To better ensure that our results neither diminish nor over-represent orbital variability, two separate
95 chronologies are considered, based on orbitally-tuned and depth-derived records (Lisiecki and Raymo,
96 2005; Huybers, 2007) . Details of depth-age relationships are given in Appendix A.

97 3. Indeterminate precession estimates from spectral analysis

98 3.1. *Method*

99 Following the convention of past studies (Hays et al., 1976; Imbrie and Imbrie, 1980), we first attempt
100 to quantify orbital forcing of early Pleistocene glacial cycles using spectral analysis, evaluating the
101 rate-of-change of $\delta^{18}\text{O}$, i.e., $d\delta^{18}\text{O}/dt$. Analysis of the rate of change, rather than the magnitude,
102 follows from major ice sheets having long response times (Weertman, 1964) and is supported by co-
103 herence between $d\delta^{18}\text{O}/dt$ and summer-integrated energy in the obliquity band (Roe, 2006; Huybers,
104 2006). Analyzing $d\delta^{18}\text{O}/dt$ also permits for better separating sensitivity to orbital forcing from the

Age model Record	σ , ‰, 2-1 Ma	Lat., °	Lon., °	Orbitally-tuned, 3-1 Ma		Depth-Derived, 2-1 Ma		Original Reference(s)
				Age, Ma	Δt , ky	Age, Ma	Δt , ky	
L2H19	0.37	50N*	24*W	3.00	0.97	2.0	0.48	Channell et al. (2016); Hodell and Channell (2016) ; Obrochta et al. (2014); Bolton et al. (2010)
LR04	0.28	-	-	3.00	2.35	-	-	Lisiecki and Raymo (2007)
H07	0.25	-	-	-	-	2.00	1.00	Huybers (2007)
DSDP 607	0.35	41N	33W	3.00	3.89	2.00	3.55	Ruddiman et al. (1989)
ODP 677	0.31	1N	84W	2.60	1.74	1.95	1.63	Shackleton et al. (1990)
ODP 846	0.29	3S	91W	3.00	2.36	1.77	2.71	Mix et al. (1995a)
ODP 849	0.29	0	111W	3.00	3.20	2.00	3.49	Mix et al. (1995b)
ODP 980/981	0.34	55N	17W	3.00	2.08	1.95	2.85	Oppo et al. (1998); McManus et al. (1999); Mc Intyre et al. (1999); Flower et al. (2000); Raymo et al. (2004)

Table 1: Properties of marine sediment cores. Listed are the standard deviation of $\delta^{18}\text{O}$ between 2 and 1 Ma, location, estimated age of the oldest sample, and mean sampling interval. Age and sampling interval are given as available for both orbitally-tuned and depth-derived age models. The coordinates of L2H19 are listed as those of IODP Site U1308, but note that between 3 and 2.42 Ma, data are from Site U1313.

influence of the relative periods of orbital variations, with previous studies noting that obliquity's longer period amplifies it relative to precession when integrating a model that relates orbital forcing to the rate-of-change of ice volume (Huybers and Tziperman, 2008; Tabor et al., 2015).

$d\delta^{18}\text{O}/dt$ is constructed by taking the first-difference of $\delta^{18}\text{O}$ then dividing by the time between samples, after linearly interpolating to an even spacing of 0.5 ky. Although some samples in L2H19 are taken at smaller intervals than this, repeating the analysis using a spacing of 0.25 ky leads to only minor differences in estimates. Power spectral density (PSD) is computed using Thomson's multi-taper method with three tapers (Percival and Walden, 1993). A noise floor is estimated by fitting a power law to the PSD (see Figure 1 and Appendix B). The variance attributed to obliquity and precession is the net integral between the power spectrum and the noise floor in their respective frequency bands, defined to be $1/41 \pm 1/125 \text{ ky}^{-1}$ and $1/21 \pm 1/125 \text{ ky}^{-1}$, including negative values where the noise floor exceeds the power spectrum. The integrals are taken as a fraction of the total area under the power spectrum, then multiplied by the time series' variance. The square root of this result is reported in amplitude units of 0.001 ‰ ky^{-1} , or $\text{meg}^{-1}\text{ky}^{-1}$.

Nearly all Pleistocene records feature a red background continuum, with $\delta^{18}\text{O}$ typically following a spectral power law ranging from 0.8 to 2 that breaks down at or above $1/100 \text{ ky}^{-1}$ (Wunsch, 2003). A process following a power law of 2 may be produced by a random walk in which its value at the next time-step is the sum of its current value and a random number drawn from a Gaussian distribution. Differencing such a record therefore whitens its spectrum (Bracewell, 1986), consistent with the approximately flat noise floor in $d\delta^{18}\text{O}/dt$ (Figure 1).

The 95% confidence interval for the power spectrum is estimated from the approximate χ^2 -distribution of the spectral estimator (Percival and Walden, 1993), with further details given in Appendix B. To obtain approximate upper 95% confidence bounds for orbital amplitudes, the procedure for calculating orbital amplitudes is applied to the upper confidence bound of the power spectrum, and vice-versa for the lower bound. For the power spectrum area used as the denominator, power is

130 taken as the central estimate, except in the orbital band where it is taken as the upper or lower
 131 95% confidence bound of the power spectrum. Where a ratio of precession to obliquity amplitude
 132 is reported, the upper and lower 95% intervals are approximated by dividing the upper and lower
 133 precession estimate by the central obliquity estimate.

134 *3.2. Spectral estimates of orbital forcing amplitudes*

135 We divide records into segments representing 3-2 Ma and 2-1 Ma to allow direct comparison with
 136 depth-derived records, which end at or near 2 Ma. Spectral amplitude estimates do not rule out the
 137 possibility of significant early Pleistocene precession forcing, but substantial uncertainties preclude
 138 a confident interpretation of results.

139 Averaged from 3-2 Ma, the estimated precession amplitude in the orbitally-tuned L2H19 is 6.8
 140 (0.0-16.8 95% confidence interval) $\text{meg}^{-1}\text{ky}^{-1}$, compared with an obliquity amplitude of 30.7 (22.9-
 141 42.1) $\text{meg}^{-1}\text{ky}^{-1}$, giving a precession-to-obliquity amplitude ratio of 0.22 (0.00 - 0.55). Over 2
 142 to 1 Ma, the precession amplitude averages a larger 24.0 (13.4-38.6) $\text{meg}^{-1}\text{ky}^{-1}$ and, unlike in the
 143 previous million years, is statistically significant. A much smaller increase in the obliquity amplitude
 144 of 4.4 $\text{meg}^{-1}\text{ky}^{-1}$ is observed between the two time periods, such that the precession-to-obliquity
 145 amplitude ratio increases to 0.68 (0.38-1.10) in the later interval.

146 Spectral estimates in other records follow a similar pattern to L2H19 (Table 2). No orbitally-tuned
 147 records give a significant precession amplitude estimate between 3 and 2 Ma. Between 2 and 1
 148 Ma, the presence of precession is more ambiguous, with four out of six tuned records – DSDP
 149 607, ODP 846, ODP 849, and the LR04 stack – giving significant precession amplitude estimates.
 150 When evaluating records on the depth-derived chronology between 2 and 1 Ma, the importance of
 151 precession is even less clear, with only two records, L2H19 and the LR04 stack, giving significant
 152 spectral estimates of precession.

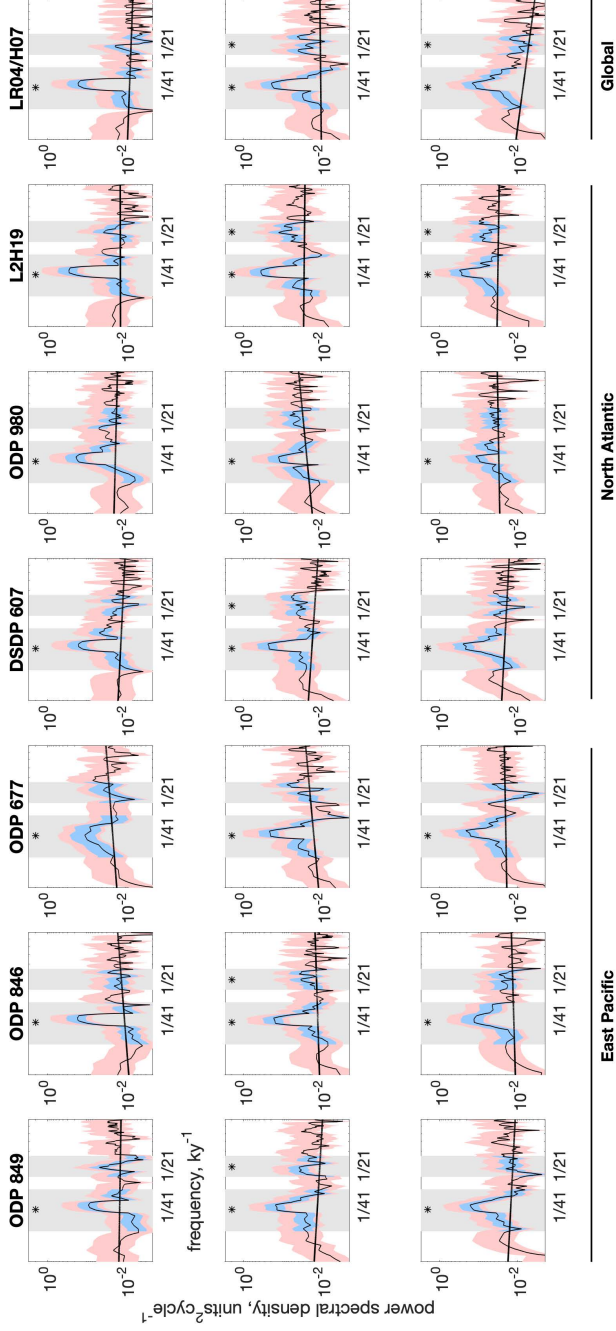


Figure 1: Power spectra of $d\delta^{18}\text{O}/dt$. Columns are organized by the longitude associated with each record from west to east, and rows according to spectra using orbitally-tuned timescales for 3-2 Ma (top), orbitally-tuned timescales for 2-1 Ma (middle), and depth-derived timescales for 2-1 Ma (bottom). The 95% confidence interval is indicated as estimated for individual spectral estimates (red) and for summing energy across the orbital band (blue; see Appendix B). Bands over which obliquity and precession power are summed (gray shading) are at $1/41 \pm 1/125 \text{ ky}^{-1}$ and $1/21 \pm 1/125 \text{ ky}^{-1}$. All twenty-one obliquity-band spectral power estimates are significant at the 95% confidence level (indicated by black stars), but only seven indicate correspondingly significant climatic precession. In the last column, the upper two panels refer to the LR04 stack, and the bottom panel refers to the H07 stack.

153 Further ambiguity arises from precession’s upper bound being poorly constrained. While only 7 of the
154 21 time-series evaluated give significant spectral estimates of precession, the upper 95% confidence
155 limit on the precession estimate is greater than obliquity’s lower 95% limit in four tuned records
156 between 3 and 2 Ma, every tuned record between 2 and 1 Ma, and two records on the depth-derived
157 timescale between 2 and 1 Ma, such that it is not always possible to rule out precession having a
158 larger amplitude than obliquity.

159 It could be that Fourier-based estimation is sub-optimal for determining orbital amplitudes on ac-
160 count of several basic assumptions being violated. The precession signal does not appear stationary,
161 as is implicitly assumed, with an apparently growing amplitude over the Pleistocene. Furthermore,
162 major frequency modulations associated with precession, such as those induced by variations in
163 eccentricity’s amplitude (Burns, 1976), lend ambiguity to the energy band within which the preces-
164 sion signal is contained. It is also clear from Table 2 that L2H19’s orbital amplitude estimates are
165 substantially larger than for other records over 2-1 Ma, and possible reasons for orbital amplitude
166 differences between records are addressed in sections 4.2 and 7.1.

167 None of these factors necessarily explain why some records give statistically significant precession
168 where others on the same chronology or across the same time interval do not. On one hand, we are
169 concerned that assessing multiple records can lead to false positives and, on the other, that the high
170 degree of variability in spectral estimates implies that the presence of significant precession cannot
171 be ruled out. These considerations prompt our exploring a complimentary method for assessing
172 whether precession variability is present in the early Pleistocene.

173 4. Empirical Nonlinear Orbital Fitting (ENOF)

174 In developing a method that is complimentary to spectral analysis, we seek to utilize precession’s
175 known frequency and amplitude modulations and to allow for non-stationarity in the amplitude of

Age model Method	Orbitally-tuned, 3-2 Ma					
	Power Spectrum			ENOF		
Forcing term	Obliquity	Precession	Precession	Obliquity	Precession	Precession
L2H19	30.7 (22.9 - 42.1)	6.8 (0.0-16.8)		31.0 (24.1-38.1)	8.6 (3.9-14.7)	
LR04	24.7 (19.1-31.8)	2.7 (0.0-10.8)		23.5 (18.5-28.6)	7.0 (3.4-11.6)	
DSDP 607	27.2 (19.9 - 36.4)	6.5 (0.0-16.1)		24.0 (18.4-30.1)	8.3 (3.5-14.1)	
ODP 677	23.3 (12.0 - 40.3)	0.0 (0.0-22.2)		21.2 (12.0-31.3)	3.8 (0.0-12.3)	
ODP 846	23.7 (16.8 - 33.6)	6.9 (0.0-17.1)		21.5 (14.9-28.6)	7.8 (2.9-14.5)	
ODP 849	14.6 (6.4 - 23.9)	5.8 (0.0-16.2)		16.4 (9.4-23.6)	5.6 (0.7-12.0)	
ODP 980/1	24.9 (17.0 - 35.4)	9.3 (0.0-19.7)		25.0 (17.9-32.4)	10.4 (5.3-17.0)	
Age model Method	Depth-derived, 2-1 Ma					
	Power Spectrum			ENOF		
Forcing term	Obliquity	Precession	Precession	Obliquity	Precession	Precession
L2H19	35.1 (24.1 - 52.0)	24.0 (13.4 - 38.6)		34.5 (24.2-45.1)	22.4 (14.0-31.7)	17.6 (9.7-27.0)
LR04	26.9 (20.2 - 36.2)	15.8 (9.4 - 24.2)		25.4 (19.2-31.9)	15.8 (10.2-21.9)	
H07	-	-		-	-	-
DSDP 607	28.7 (20.5 - 39.8)	20.8 (13.3 - 30.9)		28.8 (22.1-36.0)	19.6 (13.8-26.1)	6.8 (4.1-10.5)
ODP 677	27.5 (19.4 - 39.8)	14.2 (0.0 - 25.8)		25.5 (16.6-34.8)	16.3 (8.9-24.9)	6.4 (2.3-13.4)
ODP 846	25.4 (18.0 - 36.0)	12.6 (2.3 - 22.3)		22.6 (16.6-29.5)	13.6 (7.6-20.5)	5.7 (1.3-12.6)
ODP 849	24.7 (17.9 - 33.4)	13.8 (6.6 - 22.1)		23.9 (17.9-30.3)	13.7 (8.6-19.5)	9.2 (5.0-14.7)
ODP 980/1	19.4 (9.7 - 32.1)	12.2 (0.0 - 26.3)		17.7 (8.4-28.5)	10.5 (2.0-20.9)	6.9 (2.5-13.0)
						7.2 (0.4-16.8)

Table 2: Amplitudes of obliquity and precession contributions from spectral and ENOF estimates. Bracketed values give approximate 95% confidence

intervals, estimates are in units of $\text{mag}^{-1}\text{ky}^{-1}$, and bold font indicates statistical significance. Power spectral estimates reported here are equivalent to those shown in Figure 1. 95% confidence intervals are narrower for ENOF than for spectral analysis, such that ENOF estimates differ from spectral estimates in indicating significant precession contributions.

the precession response over time. The method we propose below is similar to spectral analysis, which can be represented as a least-squares fit of sinusoids to a time-series (e.g. Bracewell, 1986), but modified to be a least-squares fit of the orbital elements themselves that is sequentially fit using a sliding window.

4.1. Method

Previous studies have represented the orbital influence on glacial mass balance using a flexible index consisting of a weighted sum of obliquity and climatic precession (e.g. Imbrie and Imbrie, 1980), where selecting appropriate weights and climatic precession phase allows for reproducing most parameterizations of insolation forcing. Equating this index to the rate-of-change of $\delta^{18}\text{O}$ has been shown to produce a good fit in the late Pleistocene (Imbrie and Imbrie, 1980; Roe, 2006) for the same reasons given in section 3.1. Following these previous studies, we posit a functional form for the orbital forcing of ice sheet mass balance as,

$$\frac{dV}{dt} = A_o(t)\varepsilon(t - \Delta t_o) + A_p(t)e \sin(\varpi(t - \Delta t_p)) + \eta(t). \quad (1)$$

The rate-of-change of ice volume, dV/dt , is represented as a combination of obliquity, ε , and climatic precession forcing. Climatic precession has an amplitude controlled by orbital eccentricity, e , and phase equal to the longitude of perihelion, ϖ , taken relative to the fixed vernal equinox. A_p and A_o are the amplitudes respectively associated with obliquity and precession, Δt_o and Δt_p are the respective time offsets, and all four parameters are permitted to vary over time. Time offsets arise from age model error, the seasonal sensitivity of $\delta^{18}\text{O}$, and lags in the response to orbital forcing. Noise and processes not otherwise accounted for are represented by η . The values used for e , ϖ , and ε are from Berger and Loutre (1991).

Taking ϖ relative to the vernal equinox gives a model in which $\Delta t_p = 0$ implies that maximum rates of melting and ocean warming occur when perihelion aligns with Northern Hemisphere summer

198 solstice. Initial estimates for A_p , A_o , Δt_p and Δt_o are all set to zero, consistent with the rate-
 199 of-change of $\delta^{18}\text{O}$ being in phase with peak Northern Hemisphere summer intensity, but Δt_p and
 200 Δt_o could allow for precession variability of essentially any phase because they are allowed to vary
 201 within ± 10 ky. No parameter is needed for a direct offset in the precession angle ϖ , because the
 202 time offset Δt_p captures virtually all of the structure that such a parameter might introduce. Note
 203 that a positive value of Δt_p or Δt_o indicates that observations lag orbital variations, and a negative
 204 value indicates a lead.

205 Values of A_p , A_o , Δt_p and Δt_o are estimated by a nonlinear least-squares fit of equation 1 to $d\delta^{18}\text{O}/dt$
 206 over a box-car window of length τ ky, centered on a time t . The rate-of-change is constructed by
 207 a first-difference of $\delta^{18}\text{O}$ after linear interpolation to even spacing of 0.5 ky. As with spectral
 208 analysis, using a finer interpolation scheme for L2H19 only produces small changes in estimates.
 209 Fitting is undertaken using a Matlab optimization routine which uses a trust-region algorithm for
 210 parameter estimation (see Appendix C). Before evaluation, $d\delta^{18}\text{O}/dt$ is smoothed with a 6 ky filter
 211 to minimize the influence of noise in parameter estimation. Note that smoothing a record resolved at
 212 frequencies well above that of climatic precession is expected to minimally influence orbital energy,
 213 whereas coarsely sampling a sediment core instead aliases unresolved high-frequency energy to lower
 214 frequencies (Pisias and Mix, 1988). Each window is shifted relative to the previous by k ky, and
 215 the fit repeated, until the end of the time-series is reached. Each t is therefore associated with τ/k
 216 estimates for a parameter, which are averaged to obtain a single time-continuous estimate. Unless
 217 otherwise noted, we use $\tau = 50$ ky and $k = 5$ ky. Choosing k to be substantially less than τ permits
 218 for sufficient continuity to obtain a smooth estimate of the time-evolution of orbital amplitudes. To
 219 obtain time-averaged amplitudes for each of precession and obliquity, the square root of the variance
 220 of the first and second terms in equation 1, respectively, is taken.

221 Like in spectral analysis, the presence of background noise causes ENOF to overestimate orbital
 222 variance. The bias is a function of the signal-to-noise ratio (SNR), and is estimated from a Monte

Carlo approach in which ENOF is run against repeated realizations of synthetic time-series containing both orbital variance and noise. The bias correction, analogous to subtracting the noise floor in spectral analysis, is made by linearly interpolating the noise fraction of the total amplitude against the mean bias for that fraction, as estimated from synthetic tests (see Appendix D).

95% parameter confidence intervals for A_p and A_o are approximated under an assumption of asymptotic normality of the estimator, with further information given in Appendix C. Similarly to spectral analysis, when reporting a ratio of precession to obliquity amplitudes, the accompanying confidence interval comprises the lower and upper 95% confidence bounds for precession divided by the central obliquity estimate. Because estimates of Δt_p and Δt_o are strongly influenced by age model error and bound-constrained to avoid overfitting, confidence intervals are not expected to be informative for these parameters and are therefore not estimated.

4.2. Time-averaged orbital forcing amplitudes and time offsets

Unlike with spectral analysis, ENOF estimates of the precession amplitude in L2H19 are significant throughout the full 3-1 Ma period. Between 3 and 2 Ma, ENOF gives a precession amplitude of 8.6 (3.9-14.7) $\text{meg}^{-1}\text{ky}^{-1}$ and an obliquity amplitude of 31.0 (24.1-38.1) $\text{meg}^{-1}\text{ky}^{-1}$, which together yield a precession-to-obliquity ratio of 0.28 (0.13-0.47). The precession estimate rises to 22.4 (14.0-31.7) between 2 and 1 Ma, whereas the obliquity amplitude increases by only 3.5 $\text{meg}^{-1}\text{ky}^{-1}$, such that their ratio rises to 0.65 (0.41-0.92) between 2 and 1 Ma (Table 2).

The apparent detection of significant precession in the 3-2 Ma interval is supported by ENOF estimates in other records, with all but one orbitally-tuned record giving significant precession estimates over this time period (Table 2). Confidence in the significance of precession in the early Pleistocene is bolstered by a finding that ENOF precession estimates are significant in every record on both the orbitally-tuned and depth-derived chronologies between 2 and 1 Ma. Note, however, that central estimates of the precession-to-obliquity amplitude ratio average 50% lower in depth-derived records

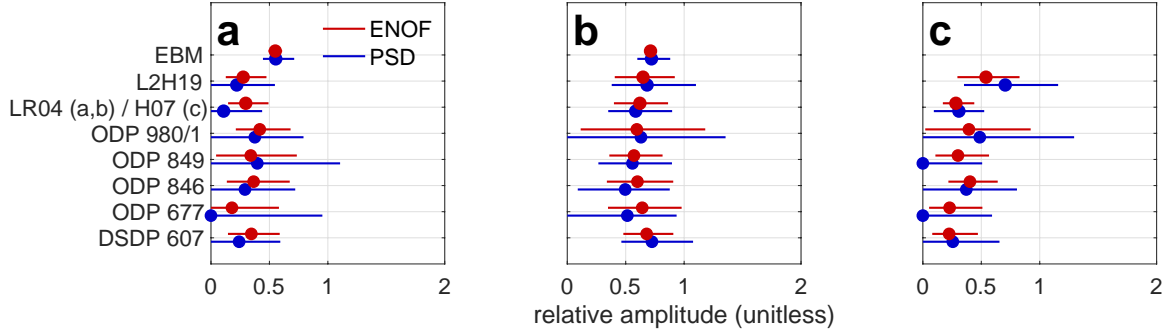


Figure 2: Precession amplitude relative to obliquity in early Pleistocene benthic $d\delta^{18}O/dt$, as estimated by ENOF (red) and spectral analysis (blue), in (a) orbitally-tuned records for 3-2 Ma, (b) orbitally-tuned records for 2-1 Ma, and (c) depth-derived records for 2-1 Ma. Circles represent best estimates, and bars represent the 95% confidence range. Estimates from ice sheet model results described in section 6 are also included. The label for the composite records, “LR04 (a,b) / H07 (c)”, refers to the LR04 stack in panels (a) and (b), and the H07 stack in panel (c).

relative to orbitally-tuned records (Figure 2b,c). Differences in precession estimates between age models is further discussed in section 7.1.

As is the case with spectral analysis, L2H19 features significantly larger orbital amplitudes than other records (see Table 2). More generally, orbital amplitudes are systematically higher in North Atlantic records than in Pacific records, and this may partly reflect greater variance from deep-water temperature in North Atlantic benthic $\delta^{18}O$ records (Duplessy et al., 1980; Waelbroeck et al., 2002). There does not appear to be a substantial difference in the relative sensitivity to precession versus obliquity between basins, with the ratio between the two averaging 0.64 for North Atlantic and 0.60 for Eastern Pacific orbitally-tuned records between 2 and 1 Ma.

The estimated time offsets, Δt_p and Δt_o , serve to quantify the timing of orbitally-induced variations in $\delta^{18}O$. Several factors make it unwise to place much weight on individual time offset estimates, however, including (i) that age uncertainties are up to half the period of precession (Huybers, 2007), (ii) that there remains significant uncertainty regarding what controls the precession phase in global

climate records (e.g. Kawamura et al., 2007), (iii) that orbitally-tuned records have previously been aligned to a Northern Hemisphere ice-volume curve, and (iv) that the ENOF model is centered about a Northern Hemisphere summer forcing. Despite these factors, agreement in Δt_p and Δt_o across several records and age models would provide confidence that the estimated precession variability represents a consistent set of physical processes.

Mean Δt_p is no more than ± 1 ky in records on both age models and over both 3-2 Ma and 2-1 Ma. In orbitally-tuned records, Δt_p averages -0.2 ky between 3 and 2 Ma, and 0.1 ky between 2 and 1 Ma, and in depth-derived records, Δt_p averages 0.5 ky between 2 and 1 Ma. Similarly, mean Δt_o does not exceed 3 ky in any record on either age model, averaging 0.5 ky over 3-2 Ma and 1.6 ky over 2-1 Ma in orbitally-tuned records, and 2.4 ky over 2-1 Ma in depth-derived records. Given age uncertainties of ± 6 ky for tuned records (Lisiecki and Raymo, 2005) and ± 10 ky for depth-derived records (Huybers, 2007), Δt_p and Δt_o in $d\delta^{18}\text{O}/dt$ may be interpreted as being indistinguishable from in-phase with the intensity of Northern Hemisphere summer.

The algorithm may occasionally fail to adequately search the parameter space, returning a Δt_p value equal to its initial estimate, though this may also occur if the initial estimate is optimal. Excluding values of Δt_p that are equal to the initial estimate before averaging does not lead in qualitatively different results, with all records giving a mean Δt_p of less than 2 ky and a mean Δt_o less than 3.5 ky.

5. Detailed analysis of orbital forcing in L2H19

An analysis of the temporal variability and trends in the estimated precession component of benthic $\delta^{18}\text{O}$ would further inform the physical origin of the signal and whether it can confidently be attributed to precession forcing. Of the records we have evaluated, L2H19 has the highest sampling resolution by a wide margin (Table 1) and features high sedimentation rates through the Pleistocene

283 (Channell et al., 2016; Hodell and Channell, 2016). In light of these exceptional properties, we are
284 motivated to more closely evaluate Pleistocene precession variability using L2H19.

285 5.1. *Further evidence for precession forcing in early Pleistocene benthic $\delta^{18}O$*

286 A common method for testing whether precession-band variance in a $\delta^{18}O$ record is of physical
287 origin is to pass the record through a narrow band-pass filter admitting only precession frequencies,
288 typically $1/18 \text{ ky}^{-1}$ to $1/24 \text{ ky}^{-1}$, and measure the correlation of the filtered signal’s amplitude with
289 that of eccentricity (e.g. Shackleton et al., 1990). Filtering can produce eccentricity-like amplitude
290 modulations in orbitally-tuned records even when no relationship with eccentricity exists (Huybers
291 and Aharonson, 2010), though methods have been proposed to overcome this problem. Zeeden et al.
292 (2015) proposed that filtering records using a wider band, e.g. $1/8$ to $1/35 \text{ ky}^{-1}$, then calculating the
293 instantaneous amplitude of the filtered time-series using the Hilbert transform and smoothing the
294 resulting curve, permits for avoiding spurious detections of eccentricity modulation. ENOF offers a
295 simpler alternative. Undertaken fully in the time domain, ENOF does not require filtering a record
296 to identify amplitude variability over time, thereby avoiding the primary concern raised by Huybers
297 and Aharonson (2010).

298 If ENOF is repeated with eccentricity excluded from the climatic precession term of equation 1,
299 A_p is responsible for capturing all amplitude modulations of precession. The correlation of A_p
300 with eccentricity then provides an independent test for the presence of precession. Because ENOF
301 can only resolve variations on timescales equal to or longer than the length of its fitting window,
302 eccentricity is smoothed by a window of the same length prior to computing the correlation.

303 The correlation of A_p with eccentricity in the orbitally-tuned L2H19 between 3 and 1 Ma is 0.46.
304 The significance of this correlation is evaluated against a null hypothesis, $H_{0, ecc}$, that A_p varies
305 independently of eccentricity. A probability distribution associated with $H_{0, ecc}$ is formed by re-
306 peating the eccentricity-independent fit 10^4 times on phase-randomized versions of the input data.

307 Phase randomization preserves the Fourier amplitudes and power spectrum of the time-series, but
 308 destroys meaningful amplitude modulations (see Appendix E for details). The 99% significance level
 309 for $H_{0,ecc}$ is found to be 0.38, allowing for a conclusion that the eccentricity modulation in L2H19
 310 is highly significant. Variations in the window width or window shift (h or k , respectively, in sec-
 311 tion 4) only induce small variations in the correlation between eccentricity and A_p (Appendix C.2).
 312 Repeating the test with a 100-ky ENOF fitting window gives an equally significant result.

313 5.2. Trends in forcing amplitudes

314 Previous work has generally described the Pleistocene as involving a distinct transition between
 315 a “41-kyr world”, featuring apparently obliquity-dominated glacial cycles, and the later “100-kyr
 316 world”, with more strongly expressed precession (e.g. Elderfield et al., 2012). Some studies have
 317 alternately described a more gradual progression in glacial-cycle characteristics (Huybers, 2007;
 318 Lisiecki and Raymo, 2007). An ENOF fit using a 100-ky window over the past 3 Ma indicates that
 319 precession’s contribution to L2H19’s $d\delta^{18}\text{O}/dt$ rose over the Pleistocene, with no abrupt transition
 320 (Figure 3c). Precession’s amplitude increased at a rate of $(16.21 \pm 0.42) \times 10^{-3} \text{ meg}^{-1}\text{ky}^{-2}$ between
 321 3 Ma and the present, roughly five times faster than the growth rate in obliquity amplitude, $(2.82 \pm$
 322 $0.29) \times 10^{-3} \text{ meg}^{-1}\text{ky}^{-2}$ (Figure 3). These results accord with an earlier finding that the spectral
 323 power of precession-band frequencies in $\delta^{18}\text{O}$ increases in amplitude over the Pleistocene (Lisiecki
 324 and Raymo, 2007). Note that eccentricity itself has slightly larger amplitude on average in the late
 325 Pleistocene, but recomputing the precession amplitude trend using a linearly de-trended eccentricity
 326 negligibly changes the result.

327 The residual between the ENOF fit and $d\delta^{18}\text{O}/dt$ gradually increases between 3 and 1 Ma, a trend
 328 that can largely be explained by an increase in the variance of $d\delta^{18}\text{O}/dt$ over the same interval. A
 329 linear regression between the moving variance of $d\delta^{18}\text{O}/dt$ and the moving variance of the ENOF
 330 residual using a box-car window of 250 ky yields an R^2 of 0.91. Additional amplitude variability

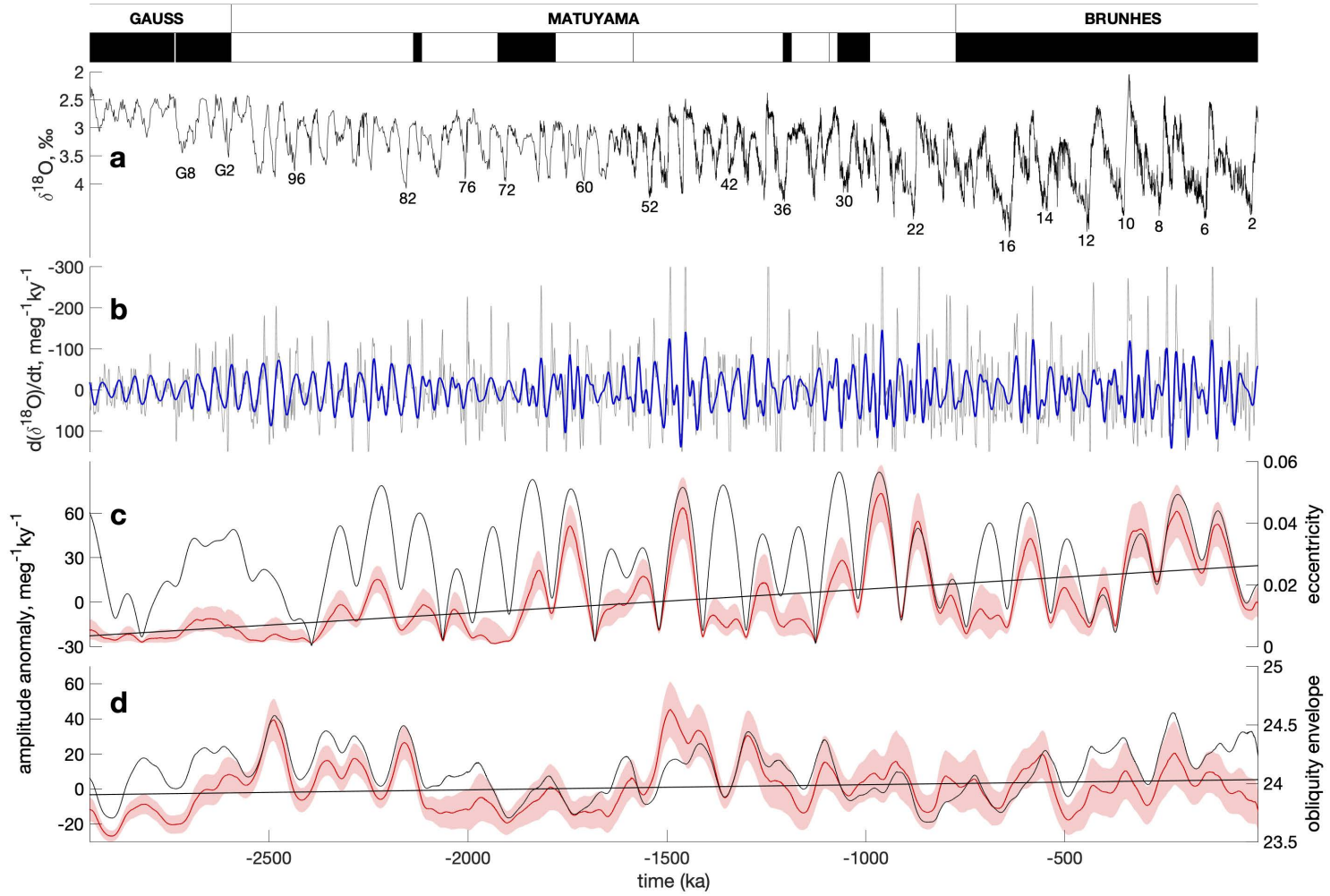


Figure 3: Trends in orbital forcing in $d\delta^{18}\text{O}/dt$ owing to precession and obliquity over the Pleistocene and late Pliocene, using data from L2H19, a high-resolution benthic $\delta^{18}\text{O}$ record. **(a)** L2H19, with select Marine Isotope Stages labeled, and its geomagnetic polarity reversal stratigraphy (Channell et al., 2008, 2016). **(b)** The rate-of-change of $\delta^{18}\text{O}$, smoothed with a 6ky 2nd-order Butterworth filter (gray), and ENOF fit to the time-series (blue) **(c)** Envelope of the precession contribution from 3 to 0 Ma (red line) and orbital eccentricity (black line). **(d)** same as (c), but for obliquity, and where the black line represents the envelope of obliquity. Envelopes are calculated as the magnitude of the Hilbert transform of the ENOF-estimated precession and obliquity contributions, and for the calculated values of obliquity. Shaded areas represent the 95% confidence intervals, and black trend-lines indicate a linear least-squares fit. The ENOF fit uses a 100 ky window, but results are similar when using a 50 ky window (see Appendix C). The y -axis is reversed in panels (a) and (b).

331 is superimposed upon precession’s amplitude trend due to its modulation by eccentricity, as can
332 be recognized in the time domain. For example, the peak at 1.75 Ma in Figure 3a apparently
333 corresponds to a strong precession peak during an eccentricity maximum.

334 6. Predictions of an ice sheet and energy-balance model

335 To examine a possible physical explanation for the observed orbital ratios in benthic $\delta^{18}\text{O}$ records and
336 the gradual increase in precession amplitude relative to obliquity, we revisit the coupled Northern
337 Hemisphere ice sheet and energy-balance model of Huybers and Tziperman (2008), hereafter the
338 EBM. The EBM represents a parabolic ice sheet in a two-dimensional transect from the equator to
339 the North Pole, and is forced with diurnally averaged daily insolation across all latitudes, permitting
340 it to capture the full seasonal temperature cycle. The model computes heat fluxes across a two-
341 layer atmosphere and a subsurface layer, with an ice sheet that freely deforms in accordance with a
342 shallow-ice approximation and sits above a deformable sediment layer.

343 A number of important factors are not included. There is no ocean, and the model does not
344 simulate geochemical interactions such as those that may drive a CO_2 feedback (Broecker, 1982),
345 nor the possible influence of sea ice (Gildor and Tziperman, 2000) or orbitally-forced fluctuations in
346 the volume of the Antarctic ice sheet (Raymo et al., 2006). Though these limitations are important
347 to note, the model has been shown to produce ice-volume variability that was previously interpreted
348 to contain little precession (Huybers and Tziperman, 2008), allowing us to evaluate the EBM output
349 in the same context as the observations.

350 6.1. *Orbital forcing in a two-million year model run with a cooling atmosphere*

351 We analyze a single run of the EBM starting at 3.1 Ma, the first 100 ky of which is excluded from
352 analysis as an equilibration period, using the parameters listed in Appendix F (Figure 4). A cooling

353 of the background climate is imposed for consistency with an observed long-term cooling trend. To
354 impose this cooling, the height of the atmospheric radiation emission level is linearly lowered from
355 7.20 km to 7.06 km between 3.1 and 1 Ma, which cools the Northern Hemisphere surface temperature
356 by 2.2°C. Cooling averaged between 45°N and 70°N is 2.7°C, consistent with an estimated North
357 Atlantic sea-surface-temperature cooling of 2.8°C over 3 to 1 Ma (Lawrence et al., 2010).

358 Orbital forcing amplitudes are estimated from differenced ice volume, and only ENOF results are
359 reported because spectral analysis produces very similar central estimates, giving precession-to-
360 obliquity amplitude ratios within 0.01 of those estimated from ENOF. Averaged over 3-2 Ma, ENOF
361 estimates a precession-to-obliquity amplitude ratio of 0.55 (0.49-0.61 95% confidence interval) in
362 simulated ice volume. This ratio exceeds that estimated in the observations, which average 0.32.
363 The ratio grows to 0.71 (0.68-0.75) between 2 and 1 Ma, a shift caused almost entirely by an
364 increase in the precession contribution. During this later interval, the partitioning of orbital energy
365 in the EBM is consistent with orbitally-tuned records, in which the ratio averages 0.62 (see Figure
366 4 for a comparison of L2H19 against simulated ice volume).

367 The upward trend in the model ice volume’s precession amplitude can be understood as an ice sheet’s
368 response to gradually cooling atmospheric temperatures. Cooling reduces melting both because of
369 a shorter melt season and less intense melting therein, leading to growth of the ice sheet and a
370 southward shift of the ablation margin. Both a shorter melt season and a more southerly melting
371 line will lead to greater precession variability (see Huybers and Tziperman (2008) and sensitivity
372 tests in Appendix F.1), where the former heightens the sensitivity to summer intensity, and the
373 latter exposes the melting line to long-term insolation variations that are more strongly influenced
374 by precession.

375 Following past approaches (Raymo and Nisancioglu, 2003; Raymo et al., 2006), we have treated $\delta^{18}\text{O}$
376 as being indicative of ice volume, though it is also sensitive to the local deep-water temperature.
377 Previous efforts to deconvolve benthic $\delta^{18}\text{O}$ into its respective components have used an inverse

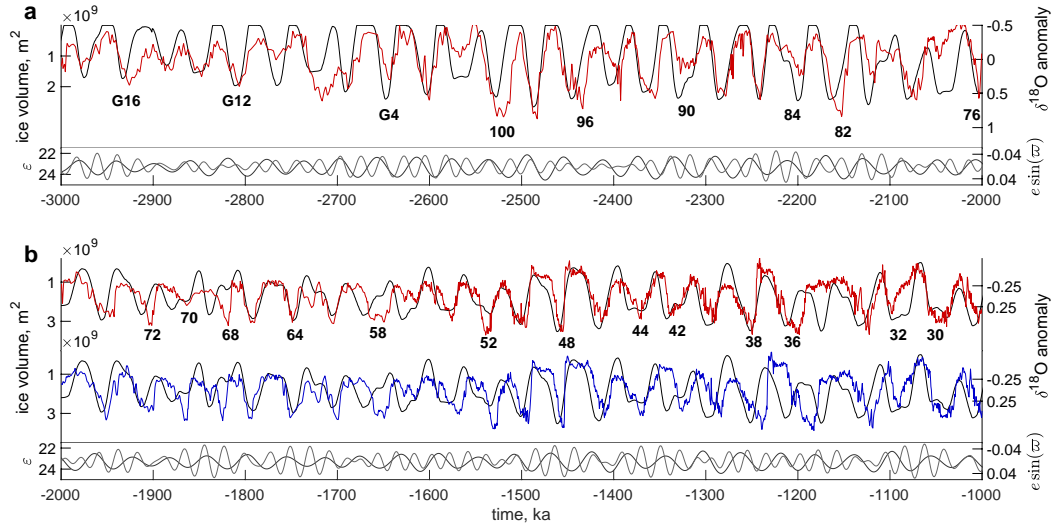


Figure 4: Simulated variations in ice volume between 3 and 1 Ma. **(a)** Model ice volume (black) and L2H19 on an orbitally-tuned age scale (red) for 3-2 Ma. Variations in obliquity (black) and the climatic precession parameter ($e \sin(\varpi)$, light gray) are below. **(b)** Similar to (a) but for 2-1 Ma and with L2H19 also shown on a depth-derived age scale (blue). $\delta^{18}\text{O}$ values are de-trended over each 1 Ma segment. Select Marine Isotope Stages are labeled for reference.

378 model of an ice sheet couple to a simplified representation of deep-water temperature (e.g. Bintanja
 379 and van de Wal, 2008) or empirical isolation of the temperature component from independent mea-
 380 surements of calcite Mg/Ca ratios (e.g. Elderfield et al., 2012). There remain large uncertainties in
 381 the relative amplitudes of ice volume and deep-water temperature in benthic $\delta^{18}\text{O}$, however (Bin-
 382 tanja et al., 2005), making it difficult to produce a pure ice-volume curve from which to directly
 383 estimate orbital forcing. The phase of precession in any such deconvolution is also uncertain because
 384 it is sensitive to factors including the lag in the response to orbital forcing, amplitude of Southern
 385 Hemisphere contributions, and seasonal sensitivity of the deep-water temperature component, each
 386 of which is uncertain.

387 7. Discussion and conclusions

388 7.1. *Differences in precession estimates across records and methods*

389 The detection and interpretation of orbital variability in climate proxies would be straightforward
 390 if orbital variations were unmodulated sinusoids, records were sampled at high resolution, sedimen-
 391 tation rates were stable across space and time, and noise and nonlinearity were small. Clearly,
 392 orbitally-induced changes in radiative forcing and the subsequent proxy recording of the response
 393 are not so simple. It is therefore unsurprising that various proxy records have engendered differ-
 394 ent interpretations when evaluated with different methods, on different chronologies, or compared
 395 against different physical models.

396 Spectral analysis detects significant precession in just 7 out of the 21 samples across records, eval-
 397 uated on two different 1 Ma intervals, and with two different age models (Table 2). In contrast,
 398 ENOF identifies a significant precession contribution in 20 out of 21 samples. The higher rates of
 399 detection with ENOF corresponds with the algorithm producing 95% confidence intervals that are,
 400 on average, 30% narrower than for spectral estimates. Higher detection rates are only physically

401 meaningful, however, if they are not borne of an increased probability of false detection. Thus, a
402 series of tests on synthetic time series are undertaken to explore differences between ENOF and
403 spectral analysis. These tests are described in Appendix D and briefly summarized here. Synthetic
404 signals are formulated by adding background noise similar to that found in the observations (Figure
405 1) with obliquity and climatic precession signals. The relative skill of ENOF versus spectral analysis
406 depends on the amplitude of the orbital signal relative to noise, and in the case of a high signal-
407 to-noise ratio, there is negligible difference between the two methods' skill (Figures D1 and D2), as
408 found in analysis of the EBM's simulated ice volume in section 6.

409 Signal-to-noise ratios are estimated for observations by dividing the total energy above the noise
410 floor in both orbital bands by the sum of all other energy in the power spectrum, giving an average
411 of 0.20 and ranging from 0.03 to 0.35 across the 21 different samples. The one exception is the
412 H07 stack for which the signal-to-noise ratio is 0.92, possibly because noise is suppressed through
413 averaging multiple records. Note that because obliquity has a larger amplitude than precession, the
414 signal-to-noise ratio for each orbital component differs, but we do not account for this distinction.
415 For a signal-to-noise ratio of 0.075, our synthetic results indicate that 95% of ENOF estimates will
416 fall within a range that is 36% narrower for ENOF than for spectral estimates, and for a signal-to-
417 noise ratio of 0.25 the range is 26% narrower. These empirical coverage intervals are thus consistent
418 with the 30% narrower confidence intervals determined for ENOF relative to spectral analysis (Table
419 2) and with ENOF having greater statistical power for identifying climatic precession.

420 In contrast to its better identifying orbital variations in the presence of noise, ENOF is relatively more
421 sensitive to age model errors than our spectral analysis approach (Figure D3). Greater sensitivity can
422 be understood in that ENOF fits only to a specific time-series of orbital forcing, whereas spectral
423 estimates are insensitive to phase shifts, and our approach of summing orbital energy across a
424 frequency band permits for recovering energy dispersed from the exact frequencies associated with
425 orbital variations. This accords with ENOF giving lower central estimates of precession amplitudes

426 than spectral analysis in all but two depth-derived records (Table 2).
 427 Estimates of the amplitude of obliquity variability are less sensitive to age model errors than pre-
 428 cession on account of its longer period leading to smaller phase differences for a given perturbation
 429 in time (Figure D3). This difference in sensitivity makes it useful to consider the ratio of precession
 430 to obliquity variability in records, but we find a surprisingly large difference in these ratios when
 431 transitioning from orbitally-tuned to depth-derived age models. Estimates of precession-to-obliquity
 432 amplitude ratios in depth-derived records average 50% lower than for orbitally-tuned records if using
 433 ENOF and 58% lower if using spectral analysis. Age errors relative to orbital variations having a
 434 standard deviation between 2 and 5 ky are only expected to decrease the precession amplitude by an
 435 average of <1% to 28% (Figure D3); age errors having a standard deviation of 10 ky is required for
 436 a >50% reduction in precession amplitude, but then a large decrease in the amplitude of obliquity
 437 is also anticipated. We speculate that orbital tuning accounts for a portion of the otherwise larger-
 438 than-expected decrease in orbital energy. The first step of orbital tuning for records included in the
 439 LR04 stack involves mapping $\delta^{18}\text{O}$ variations onto a target curve representing June 21 insolation
 440 at 65°N (Lisiecki and Raymo, 2005; Imbrie and Imbrie, 1980), which primarily contains climatic
 441 precession variability. Tuning $\delta^{18}\text{O}$ records to a precession target using a dynamic time warping
 442 algorithm similar to that involved in the LR04 alignment procedure has been shown to artificially
 443 increase estimates of the precession amplitude (Proistosescu et al., 2012). The combination of depth-
 444 derived ages being untuned and their containing age errors may account for estimates of precession
 445 amplitude being much smaller when using depth-derived as opposed to orbitally-tuned ages.
 446 A final consideration for differences in orbital amplitudes relates to variable sampling resolution
 447 across records. Coarsely sampling marine sediment records aliases high-frequency variability into
 448 lower-frequency bands (Pisias and Mix, 1988). Moreover, sampling intervals above the Nyquist
 449 frequency may not suffice for fully resolving orbital variability because of uneven sampling, time un-
 450 certainty, and the amplitude and frequency modulation present in obliquity and climatic precession.

Between 2 and 1 Ma, the sampling resolution in depth-derived records vary by more than an order of magnitude, with L2H19 averaging 60 data points over a 21 ky precession cycle, and DSDP 607 averaging just 5.5 points. If L2H19 were sampled at a resolution equal to that of the DSDP 607 record, a 16% lower precession amplitude estimate would be expected from either ENOF or spectral analysis, compared to an essentially unchanged estimate of the obliquity amplitude (Figure D5). Although possibly only a coincidence, the DSDP 607 estimate of the amplitude of precession using the orbitally-tuned age model is, in fact, 15% lower than for L2H19, where both records are from the North Atlantic and obtained at similar water depths.

7.2. Interpretation of orbital amplitudes and trends

Despite some evidence for the presence of precession in early Pleistocene glacial cycles (e.g. Lisiecki and Raymo, 2007), a long-standing view has persisted that precession variability in early Pleistocene benthic $\delta^{18}\text{O}$ is mostly negligible in amplitude (Ruddiman et al., 1986), motivating explanations for obliquity-paced glacial cycles (Raymo and Nisancioglu, 2003; Loutre et al., 2004; Raymo et al., 2006; Huybers, 2006; Tabor et al., 2015). Our finding that early Pleistocene $\delta^{18}\text{O}$ records contain significant precession variability nearly in phase with Northern Hemisphere summer intensity suggests that proposed mechanisms to continuously suppress precession may be less relevant to the early Pleistocene than previously believed.

One possibility is that, in accordance with classical Milankovitch theory, glaciation is controlled by Northern Hemisphere summer insolation (Milankovitch, 1941; Huybers, 2006). In such a model, the observed gradual increase in precession amplitude (Figure 2) is explained on the basis of a southward extension of the ice sheet ablation margin induced by global cooling, making variations in ice volume more sensitive to precession. An alternative interpretation, consistent with the proposal of Murphy (1869), is that the early Pleistocene represents a transitional period in which the net precession contribution to global ice volume shifts from Southern to Northern Hemisphere dominance. Such a

475 model also holds global cooling responsible for the increase in precession amplitude, but instead im-
476 plies that anti-phased precession-forced ice volume fluctuations between hemispheres, which would
477 cause cancelation of the $\delta^{18}\text{O}$ precession signal (Raymo et al., 2006), became increasingly imbal-
478 anced from Northern Hemisphere ice sheets growing in size, and possibly, Antarctica becoming more
479 stable.

480 Neither model excludes the possible importance of other factors. For example, erosion of regolith by
481 an ice sheet (Clark and Pollard, 1998) could contribute to less frequent full deglaciations, keeping
482 the ablation zone relatively far south and exposed to precession-dominant insolation. Past efforts to
483 model the ice sheet response to real or idealized orbital forcing have yielded ice volume fluctuations
484 ranging from precession-dominant (e.g. Nisancioglu, 2004) to obliquity-dominant (e.g. Berger et al.,
485 1999). The variety in these results as well as the possible importance of mechanisms not included
486 in the EBM suggests a need for further empirical analyses and simulation to better determine the
487 characteristics of early-Pleistocene glacial variability and its causes.

488 Two further important questions have not been explored here. First, the origin of glacial cycle
489 asymmetry, which has been identified throughout the full Pleistocene (Ashkenazy and Tziperman,
490 2004; Lisiecki and Raymo, 2007), remains uncertain, and further exploration of the connections
491 between precession forcing, asymmetry, and age model accuracy would be useful. Second, it has
492 been suggested that both the phase and amplitude of Pleistocene 100-ky variability are sensitive
493 to precession (e.g. Imbrie et al., 1993). Lisiecki (2010) proposed that strong precession forcing
494 disrupts 100-ky variability in $\delta^{18}\text{O}$ over the past 5 Ma, but raised the question of “how precession
495 modulation could suppress 100-kyr glacial cycles during the early Pleistocene 41-kyr world when the
496 23-kyr power of $\delta^{18}\text{O}$ is negligible”. Caballero-Gill et al. (2019) suggested that 100-ky glaciations also
497 occurred during the Pliocene, and proposed that a nonlinear response to precession is responsible.
498 Our finding of significant early-Pleistocene precession variability suggests that further investigation
499 into the links between orbital eccentricity, precession forcing, and quasi-100-ky climate variability is

500 needed.

501 A revised description of the early Pleistocene as featuring significant and gradually increasing pre-
502 cession amplitude in phase with Northern Hemisphere summer intensity recasts the time period as
503 supporting, rather than contradicting, the long tradition of models that invoke changes in summer
504 insolation as controlling global ice volume fluctuations (Murphy, 1869; Milankovitch, 1941; Hays
505 et al., 1976; Imbrie and Imbrie, 1980; Raymo et al., 2006). Whether the early Pleistocene accords
506 more readily with the model of Milankovitch or that of Murphy remains to be seen.

507 8. Acknowledgements

508 PRL and PJH were supported by National Science Foundation award 1338832. DAH was supported
509 by Natural Environmental Research Council grant NE/R000204/1 and Engineering and Physical
510 Sciences Research Council grant EP/S030417/1. DAH thanks D. Schrag and the Harvard University
511 Center for the Environment for supporting a sabbatical during AY 2018-2019. This research used
512 samples and/or data provided by the International Ocean Discovery Program (IODP).

513 Appendices

514 Appendix A. Depth-age relationships

515 Orbitally-tuned chronologies are developed by matching to LR04. The LR04 age model is constructed
516 by alignment of the LR04 stack with the ice-volume model of Imbrie and Imbrie (1980), where ice-
517 model parameters are adjusted over time to give an increasingly asymmetric target and longer
518 response time owing to larger ice sheets. Tuning is achieved first by maximizing the correlation
519 between the stack and ice model, then further adjusting the timescale to be in phase with the ice
520 model’s obliquity component. The re-tuning to obliquity allows the precession phase to vary between
521 glacial cycles. The depth-derived approach uses the orbitally-independent age model of Huybers
522 (2007), referred to as H07. H07 is constructed by graphic correlation of 14 benthic and planktic
523 records, and alignment of synchronous geomagnetic and isotopic events across records, between
524 which age is linearly interpolated with depth after correcting for downcore compaction.

525 L2H19’s orbitally-tuned chronology is based on alignment to the LR04 stack by identification of
526 isotopic events occurring both in LR04 and L2H19, with an assumption of linear sedimentation
527 rates between them (Bolton et al., 2010; Channell et al., 2016; Hodell and Channell, 2016). The age
528 model is supplemented by correlation of sediment lightness to ODP Site 609 between the present
529 and 76 ka (Obrochta et al., 2014), and to the NGRIP record between 76 and 110.5 ka (Hodell and
530 Channell, 2016).

531 To convert L2H19 to a depth-derived timescale, it is aligned with the benthic $\delta^{18}\text{O}$ record of Site 607
532 on the H07 age model. Site 607 is chosen because it is closest geographically to the records comprising
533 L2H19, being drilled at the same location as U1313 in the North Atlantic, and is therefore likely to
534 have the most similar glacial cycles. Note, however, that the H07 age model for Site 607 is based on
535 a global calibration with other records in the H07 stack. Isotopic event ages used in calibrating H07

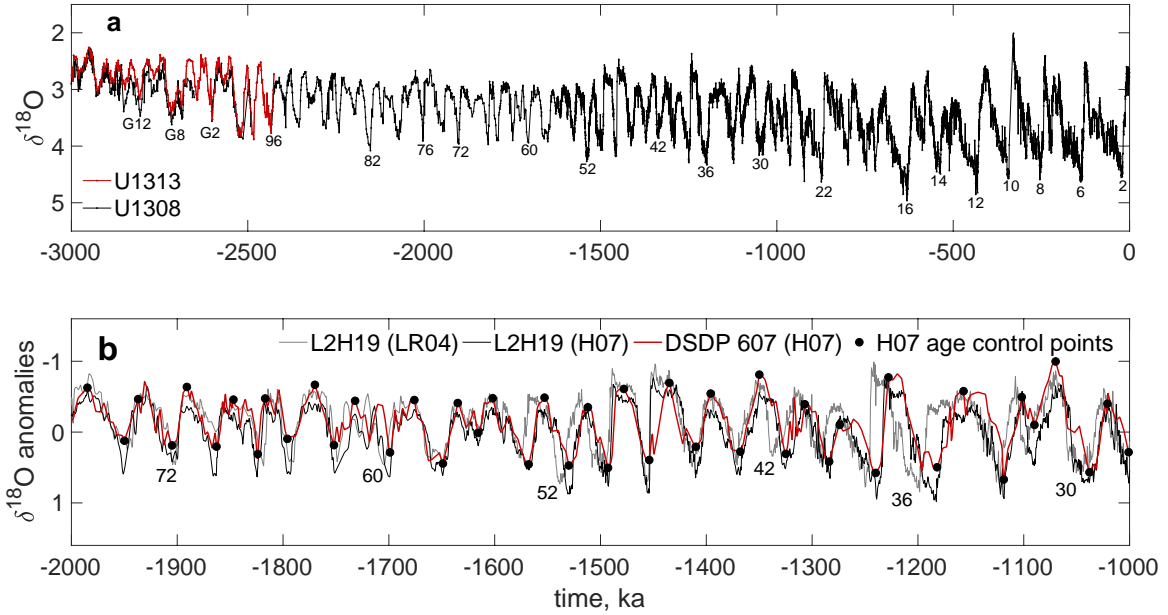


Figure A1: Pleistocene $\delta^{18}\text{O}$ records and age models for L2H19. **(a)** The orbitally-tuned L2H19 benthic $\delta^{18}\text{O}$ record comprising data from IODP Sites U1313 (red) and U1308 (black). **(b)** L2H19 (black) after alignment to a depth-derived timescale for DSDP 607 (red), where black markers are age control point used for calibration. The orbitally-tuned L2H19 is also shown (gray) for comparison. Records in panel (b) are de-trended to enable direct comparison, and select Marine Isotope Stages are labeled in both panels.

are adopted as age control points (ACPs) for L2H19, with a total of 48 events identified between 2 and 1 Ma. The ACPs of L2H19 and Site 607 were aligned by assigning to L2H19's ACPs the ages of Site 607's ACPs, then linearly interpolating age with depth between these points. Note that the depth-derived timescale ends at 2 Ma, because too few independent $\delta^{18}\text{O}$ records exist beyond 2 Ma to adequately constrain age-depth relationships without orbital assumptions. The five other individual records included in this study are also evaluated on both orbitally-tuned and depth-derived age scales, following the age models of LR04 and H07, respectively. They are used here as published in Lisiecki and Raymo (2005) and Huybers (2007).

Appendix B. Spectral estimates

All power spectra are computed with Thomson’s multi-taper method (Percival and Walden, 1993) using three tapers. The noise floor for the power spectrum is computed by a least-squares fit of a power-law,

$$y = Af^q, \tag{B.1}$$

to the power spectrum, where the parameters A and q are chosen to minimize the sum of squared residuals between y and the power spectrum. Frequencies below $1/150 \text{ ky}^{-1}$, between $1/41 \pm 1/125$, between $1/21 \pm 1/125$, and above $1/5 \text{ ky}^{-1}$ are excluded from the fit. If the net variance in a band is negative with respect to the estimated noise floor, the amplitude is assigned a value of zero. The noise floor is approximately white in the rate-of-change of $\delta^{18}\text{O}$ (Figure 1). Across all records on both the orbitally-tuned and depth-derived age models and both time intervals evaluated (3-2 Ma and 2-1 Ma), A averages 0.02 ± 0.02 and q averages -0.01 ± 0.2 , where the range represents one standard deviation.

The 95% confidence interval for power spectral density is estimated from the approximate χ^2 distribution of the spectral estimator (Percival and Walden, 1993). The interval is given by $\left[\frac{\nu S(f)}{Q_\nu(p)}, \frac{\nu S(f)}{Q_\nu(1-p)} \right]$, where S is the estimate at frequency f , ν is the equivalent degrees of freedom, and $Q_\nu(p)$ and $Q_\nu(1-p)$ are the $p = 0.025$ and $1-p = 0.975$ percentage points on the χ_ν^2 distribution with ν degrees of freedom. For an estimate at a given frequency, ν is approximately equal to $2K$ where K is the number of tapers used in the multi-taper analysis. The overall orbital amplitude estimate has more degrees of freedom, however, because it is obtained by summing energy across several spectral estimates in an orbital band. There are B_f/B_W independent spectral estimates in an orbital band, where $B_f = 2/125 \text{ ky}^{-1}$ is the width of an orbital band and B_W is the spectral bandwidth, which represents the frequency range across which spectral estimates decorrelate. An orbital amplitude estimate therefore has approximately $\frac{2KB_f}{B_W}$ degrees of freedom.

Several aspects of the confidence interval for spectral estimates are uncertain. A simple power-law representation of the noise floor (equation B.1) is assumed, and its coefficients are influenced by the choice of frequency range over which it is fit, here $1/150$ to $1/5 \text{ ky}^{-1}$. The variance of the spectral estimator is not perfectly χ^2 -distributed when deterministic variance is partially responsible for the spectral peak, as the χ^2 approximation is most accurate for a random process (Percival and Walden, 1993). To check the applicability of the approximate confidence intervals for the purposes of this study, we compute the fraction of synthetic tests, described in Appendix D, for which the true precession amplitude lies within the confidence interval. For tests with SNR=0 (pure noise), 0.075, 0.25, 0.5, 1, and 2, the estimated confidence interval contains the true amplitude in 93.8%, 97.3%, 98.5%, 99.7%, 99.99% and 100% of tests after bias correction, implying the coverage is approximately correct for noisy signals and slightly conservative for less noisy signals. The average approximate SNR of 0.20 in observations implies that the coverage interval is expected to be generally appropriate and in some cases slightly conservative. Note that for SNR<1, the confidence interval is less conservative than for ENOF (see Appendix D.1), suggesting that the relative uncertainty of spectral analysis is not being overstated in our comparison of methods.

An alternative method for estimating uncertainties is to evaluate the significance of orbital-band spectral energy relative to the expected distribution of the null hypothesis of no orbital energy. In this approach, an approximate χ^2 confidence interval is constructed for the position of the noise floor, and an orbital amplitude estimate is considered significant if the integrated energy between the power spectral density and the 95% level for the noise floor in an orbital band exceeds zero. We elect not to use this approach because it does not provide an estimate of the uncertainty range associated with the orbital amplitude estimate, only providing a measure of the estimate's statistical significance. It is nonetheless useful to verify that the use of the alternative method wouldn't lead us to different conclusions. Repeating the analysis with this method gives no significant precession amplitude estimates among orbitally-tuned records between 3 and 2 Ma, four significant estimates

592 for tuned records between 2 and 1 Ma, and one significant estimate for depth-derived records between
 593 2 and 1 Ma, similar to the zero, five, and two significant estimates, respectively, from the method
 594 we use. The slightly more conservative results in the alternative method arises from the fact that
 595 the χ^2 distribution is asymmetric, so that the difference between its 2.5th and 50th percentile is
 596 less than between its 50th and 97.5th percentile. Because confidence is assessed on the basis of an
 597 upper confidence level for the noise floor in the alternative method and a lower confidence level for
 598 the power spectrum in the method we use, the latter will tend to indicate significance more often.
 599 In our case, results from both methods are similar because the 24 degrees of freedom used makes
 600 the resulting χ^2 distribution close to symmetric.

601 Appendix C. Empirical Nonlinear Orbital Fitting (ENOF) algorithm

602 ENOF's parameter search for A_p , A_o , Δt_p and Δt_o is undertaken using a Matlab routine, "lsqcurve-
 603 fit", which uses a trust-region algorithm for optimization. The trust-region method is preferred over
 604 a Levenberg-Marquardt method because it allows us to place bound constraints on the parameter
 605 values. Δt_o and Δt_p are capped at ± 10 ky to avoid overfitting by an arbitrary phase assignment.
 606 Initial estimates are set at 0 for all parameters.

607 Being a gradient-descent method, the trust-region algorithm is not a global search of all possible
 608 parameter combinations so does not theoretically guarantee a global minimum. Such an exhaustive
 609 search is computationally prohibitive. Nonetheless, it is useful to check that the parameter space
 610 is likely smooth and without multiple local minima that could cause a gradient-descent method to
 611 converge to the wrong values. A "brute force" parameter search on a select 50 ky window reveals a
 612 smooth, elliptical parameter space with respect to the residuals, and converges toward the parameter
 613 values selected by nonlinear least squares (Figure C1).

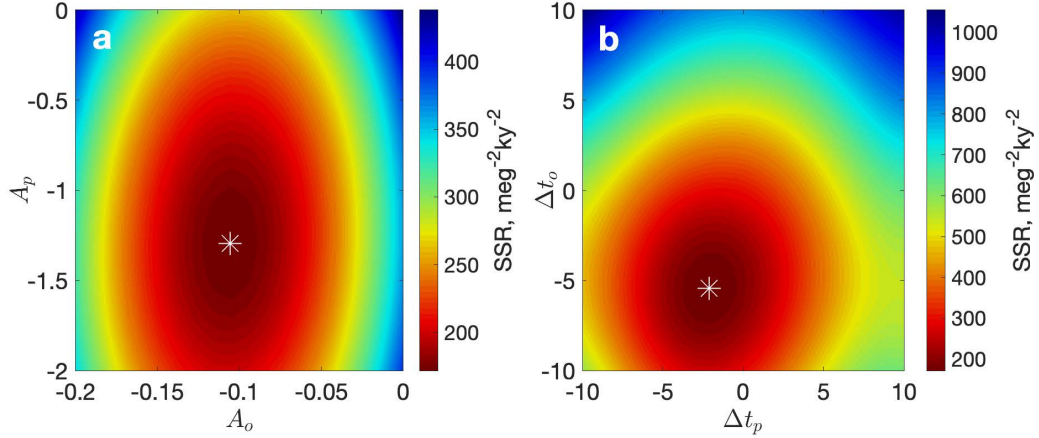


Figure C1: Comparison of nonlinear least-squares estimates to an exhaustive parameter search. **(a)** Estimates for A_p and A_o , where Δt_p and Δt_o are at the values estimated by nonlinear least-squares. The white star represents the nonlinear least-squares estimate of the best-fitting combination of parameters, and the contours represent the the sum of squared residuals computed by the brute force search. The fit is estimated over a 50ky period starting at 1.8 Ma in L2H19’s smoothed rate-of-change. **(b)** Same as (a), but for estimates of Δt_o and Δt_p , where A_p and A_o are at the values estimated by nonlinear least-squares.

614 *Appendix C.1. Parameter uncertainties and confidence intervals*

615 The 95% confidence intervals for A_p and A_o are estimated using the Matlab routine “nlparci”. They
 616 are approximated from a linearization of the nonlinear regression problem under an assumption that
 617 the estimator is asymptotically normally distributed. The approximate confidence interval is given
 618 by $\hat{\boldsymbol{\theta}}_{CI} = \hat{\boldsymbol{\theta}} \pm S_E T_{inv}(1-\alpha/2, n-p)$, where $\hat{\boldsymbol{\theta}}$ is the vector of nonlinear regression parameter estimates.
 619 S_E is the estimated standard error, and T_{inv} the Student’s T inverse cumulative distribution that
 620 is evaluated at a confidence level α with degrees of freedom equal to the number of observations,
 621 n , minus the number of model parameters, p . Here, $S_E(\hat{\boldsymbol{\theta}}_i) = s \|\mathbf{r}^i\|$, where $s = \sqrt{\frac{SSR(\hat{\boldsymbol{\theta}})}{n-p}}$. SSR
 622 is the sum of squared residuals, and \mathbf{r}^i is the i th row of the matrix \mathbf{R}^{-1} , which originates from a
 623 QR -factorization of the Jacobian matrix, $J = QR$ (see Bates and Watts, 1988). To prevent negative
 624 amplitudes, confidence intervals are truncated below zero.

It is useful to verify the coverage of ENOF’s approximate 95% confidence intervals, specifically that they are not likely to underestimate the uncertainty. A measure of validity is the fraction of the synthetic tests, described in Appendix D.1, for which the true orbital amplitude falls within the range of the estimate’s confidence interval. For synthetic time-series featuring orbital variance with SNR= 0 (pure noise), 0.075, 0.25, 0.5, 1, and 2, the 95% confidence interval for the precession amplitude contains the correct amplitude in 94.5%, 97.3%, 98.9%, 99.4%, 99.5%, and 99.6% of tests, suggesting that the confidence intervals are conservative.

Appendix C.2. Sensitivity to choice of window length and shift

It is important to verify that our results are not qualitatively sensitive to the choice of window τ , the fitting window length, and k , the distance between each overlapping windowed fit. Orbital amplitudes are estimated for L2H19 between 3 and 1 Ma when ENOF is run with different combinations of values of τ and k , respectively ranging from 50 to 100 ky and 1 to 6 ky. Using a larger value of τ tends to slightly reduce both the precession and obliquity estimates as the algorithm has less flexibility to fit against observations when attempting to fit a single amplitude value over a wider range. Changing τ from 50 ky to 100 ky reduces the precession amplitude estimate from 23.5 $\text{meg}^{-1}\text{ky}^{-1}$ to 19.7 $\text{meg}^{-1}\text{ky}^{-1}$, and the obliquity estimate from 37.0 $\text{meg}^{-1}\text{ky}^{-1}$ to 34.0 $\text{meg}^{-1}\text{ky}^{-1}$. Alternative values of τ ranging from 60 to 90 ky give proportional reductions in amplitude estimates relative to $\tau = 50\text{ky}$. Results are mostly insensitive to changes in k , with both precession and obliquity estimates changing by 0.1 $\text{meg}^{-1}\text{ky}^{-1}$ or less for values of k ranging from 1 to 6 ky.

We also repeat the eccentricity-independent test for precession, described in section 5.1, with different combinations of values of τ and k . Wider windows produce a slightly higher correlation with eccentricity because they produce smoother variations. Using $\tau = 50, 60, 70, 80, 90$, and 100 ky results in correlations of A_p with eccentricity of 0.46, 0.47, 0.49, 0.50, 0.54, and 0.55. Results are mostly insensitive to the choice of k , and repeating the tests with values of k ranging from 1 to 6

ky for each value of τ yields a change of 0.01 or less in the correlation of A_p with eccentricity. We repeated the 10^4 phase-randomized trials described in section 5.1 for $\tau = 100\text{ky}$, which give a 99% significance level of 0.51, compared to a correlation of 0.55 in L2H19, indicating that the significance of the eccentricity-independent test for precession is likely not sensitive to reasonable choices of τ or k .

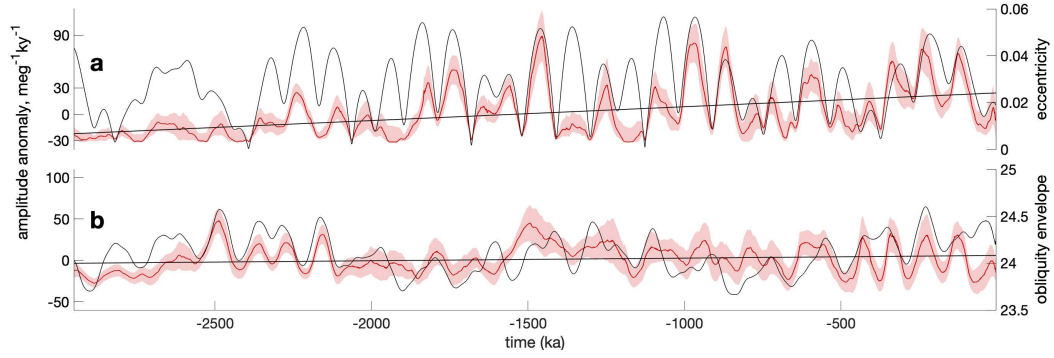


Figure C2: Trends in orbital forcing in $d\delta^{18}\text{O}/dt$ owing to precession and obliquity over the Pleistocene and late Pliocene, using data from L2H19. **(a)** Envelope of the precession contribution from 3 to 0 Ma (red line) and orbital eccentricity (black line). **(b)** same as (a), but for obliquity, and where the black line represents the envelope of obliquity. Envelopes are calculated as the magnitude of the Hilbert transform of the ENOF-estimated precession and obliquity contributions, and for the calculated values of obliquity. Shaded areas represent the 95% confidence intervals, and black trend-lines indicate a linear least-squares fit.

Appendix D. Sensitivity tests for ENOF and spectral analysis

To quantify the sensitivity of orbital amplitude estimates from both ENOF and spectral analysis to (i) the presence of background noise, (ii) the presence of age error, and (iii) differences in sampling resolution, we apply both methods to a common set of synthetic time-series with properties expected to be similar to Pleistocene $\delta^{18}\text{O}$ records.

Appendix D.1. Sensitivity to noise

Noise introduces bias in both spectral and ENOF estimates. To quantify this bias, we study estimates from both methods when applied to synthetic data. Two competing scenarios are considered in which estimates for a pure noise signal are compared with estimates for synthetic time-series featuring orbital forcing. We adopt a null hypothesis, H_0 , that orbital variability is absent, and estimate H_0 's distribution with a Monte Carlo approach, applying both methods to 2.5×10^4 realizations of noise. Red noise is initially formed following a power law of 2 with a decorrelation frequency of $1/150 \text{ ky}^{-1}$, then differenced to produce a mostly white continuum consistent with observations, as evident in Figure 1. To form probability distributions associated with the alternate hypothesis that orbital variability is present, we evaluate 2.5×10^4 synthetic time-series spanning 2 to 1 Ma featuring climatic precession and obliquity in an average amplitude ratio of 0.55, which is close to the estimated precession-to-obliquity amplitude ratio in orbitally-tuned records between 2 and 1 Ma. Noise with the same properties as in H_0 is then added to the synthetic signal. Six cases, denoted H_1 to H_6 , or H_{1-6} , are considered, for signal-to-noise ratios of 0.075, 0.25, 0.5, 1, 2, and with no noise. Signal-to-noise ratio is defined here as the variance ratio of the orbital and noise components. The variance of the realized time series, comprising both signal and noise, is fixed such that each distribution features different orbital amplitudes which approach zero as the signal-to-noise ratio approaches zero.

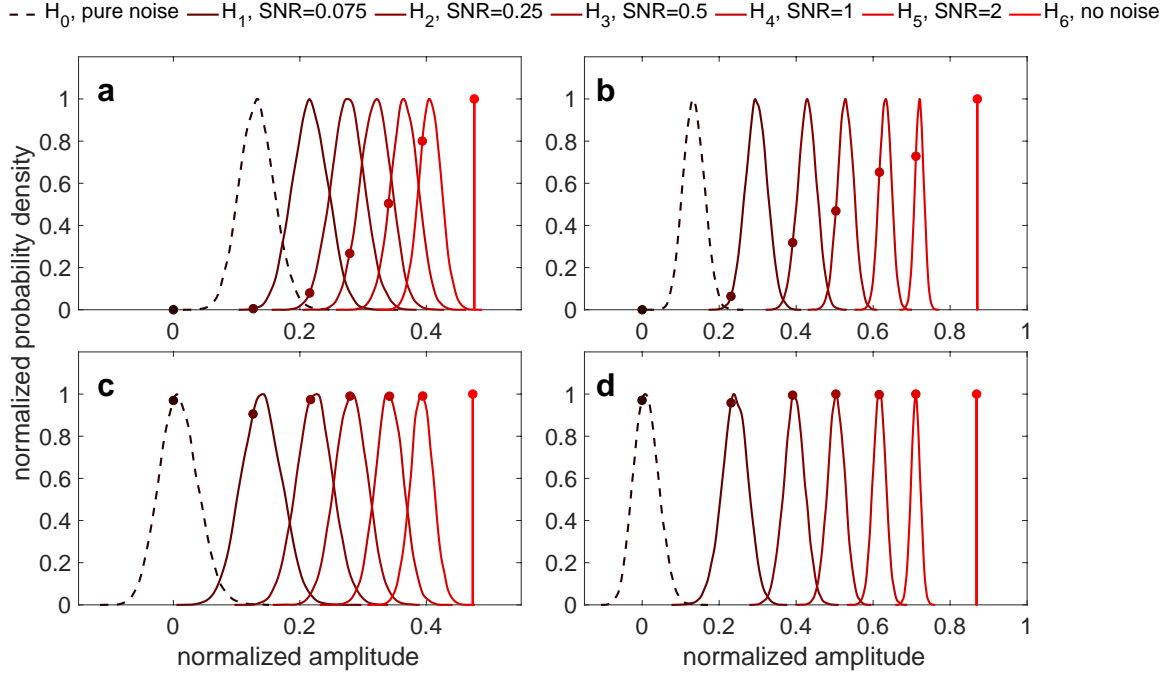


Figure D1: ENOF estimates for obliquity and precession amplitudes in tests on synthetic time-series with different signal-to-noise ratios. **(a)** Estimates for precession, taken as the square root of the variance of the first term in equation 1, before correcting for noise-induced bias, where each distribution represents 2.5×10^4 realizations. **(b)** Same as (a), but for the obliquity estimates, taken as the square root of the variance of the second term in equation 1. **(c)** Same as (a), but after applying the bias correction. **(d)** Same as (b), but after applying the bias correction.

678 In the absence of noise, H_6 , all estimates in both methods give the true amplitude. In H_{1-5} the
679 median ENOF estimate exceeds the true precession amplitude by 70%, 28%, 15%, 7%, and 3%, and
680 obliquity by 29%, 10%, 5%, 3%, and 1% (Figure D1a,b). Spectral estimates give similar biases if the
681 noise floor is not accounted for, with the median estimate exceeding the true precession amplitude
682 by 82%, 29%, 15%, 8%, and 4% and obliquity by 29%, 9%, 5%, 2%, and 1% (Figure D2a,b). These
683 biases are corrected before evaluating H_{1-6} against H_0 .

684 The bias associated with ENOF is a function of the amplitude of noise relative to the orbital
685 signal. Determining the correction requires an estimate of the noise fraction of the total amplitude,

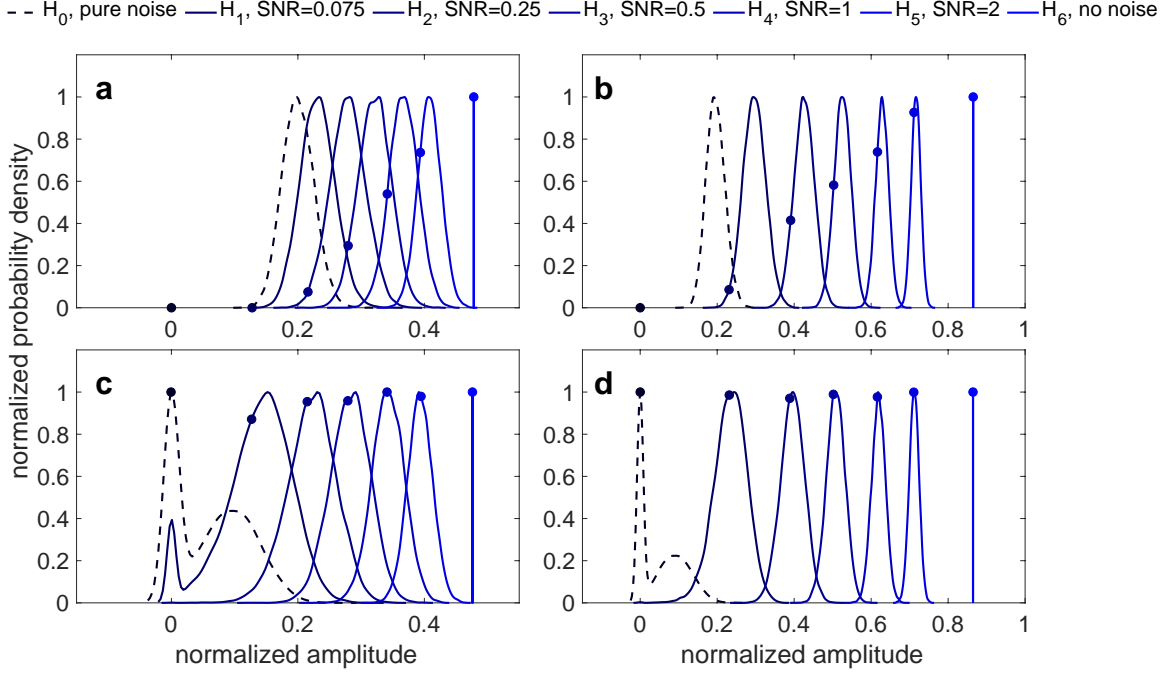


Figure D2: Spectral estimates of obliquity and precession amplitudes in synthetic tests on time-series with different signal-to-noise ratios. **(a)** Estimates for precession, as described in section 3.1, before correcting for noise-induced bias, where each distribution represents 2.5×10^4 realizations. **(b)** Same as (a), but for the obliquity estimates. **(c)** Same as (a), but after applying the bias correction. **(d)** Same as (b), but after applying the bias correction.

686 which is estimated by fitting the background continuum of the power spectrum as done for spectral
687 estimates, then computing the area below the noise level as a fraction of the total area under the
688 power spectrum and taking the square root of this value. A correction amplitude is determined by
689 linearly interpolating the noise fraction with the mean bias from synthetic tests.

690 In spectral analysis, estimates are bias-corrected by subtracting the noise floor as described in
691 Appendix B. If the variance estimate is negative, an amplitude of zero is assigned to avoid obtaining
692 a complex amplitude estimate when taking the square root of the variance. This, and the distortion
693 introduced by taking the square root of values close to zero, account for the shape of H_0 and the
694 upticks at zero in H_0 and H_1 in Figures D2c and D2d. This distortion does not occur in ENOF

estimates because the bias correction is applied after variance is converted to amplitude.

Appendix D.2. Sensitivity to age error

The introduction of age model error, which disperses orbital energy to nearby frequencies, is expected to cause underestimation bias in both methods. ENOF allows for variable time offsets from orbital variations, but typically cannot fit age error that exceeds the bounds on Δt_o and Δt_p , though it may recover some amplitude if the age model is incorrect by close to a full orbital cycle. The default bounds of ± 10 ky allow ENOF to fit almost any precession phase, but only covers half of an obliquity cycle.

10^4 synthetic time-series are generated, with age error, Δt , introduced. Background noise is added with the same properties as described in section Appendix D.1, and scaled so that time-series have a signal-to-noise ratio of 0.5. Variability in the sedimentation rate, $s(t)$, is first modeled as a random walk, i.e., $s_{n+1} = s_n + \eta_n$ where η_n is drawn from a Gaussian distribution (Huybers and Wunsch, 2004), then integrated to give variations in depth with age. Synthetic time-series span 2 to 1 Ma and, following Huybers and Wunsch (2004), age error is modeled as following a ‘Brownian bridge’, tapering to zero at each endpoint to simulate the increasing amplitude of age error with time away from age-control points. Five cases, S_{0-4} , are considered. S_0 , having no age error, is identical to H_3 in Appendix D.1. In S_{1-4} , η_n is scaled such that age model error has a standard deviation of 0, 2, 4, 5, and 10 ky.

There is little to no attenuation in obliquity amplitude estimates for either ENOF or spectral analysis in S_{1-3} . The average ENOF obliquity amplitude estimates for S_{1-3} are within 1%, 1%, and 2.2% of that for S_0 . For spectral analysis, the average obliquity attenuation relative to S_0 is less than 1% for S_{1-3} . The ENOF obliquity estimate is dramatically reduced in S_4 , however, because a standard deviation of 10ky implies age variations of $\sim \pm 20$ ky, double the range over which Δt_o and Δt_p are allowed to vary.

719 ENOF estimates of precession amplitude are generally more sensitive to age error than spectral
 720 estimates. Mean estimates for S_{1-3} are 1%, 15%, and 25% less than for spectral estimates. A
 721 regression of spectral estimates of precession amplitude against ENOF estimates in depth-derived
 722 records produces a slope of 1.07 ± 0.35 , where the range indicates the 95% confidence interval, and
 723 is consistent with the relationship predicted by S_3 , which gives a slope of 1.33 (Figure D4). Note
 724 that the age error in S_3 is lower than was independently estimated for the depth-derived age model
 725 (Huybers, 2007), but that such smaller age errors are also implied by the difference between this age
 726 model and orbitally-tuned records as well as the amplitude of the obliquity signal in depth-derived
 727 records.

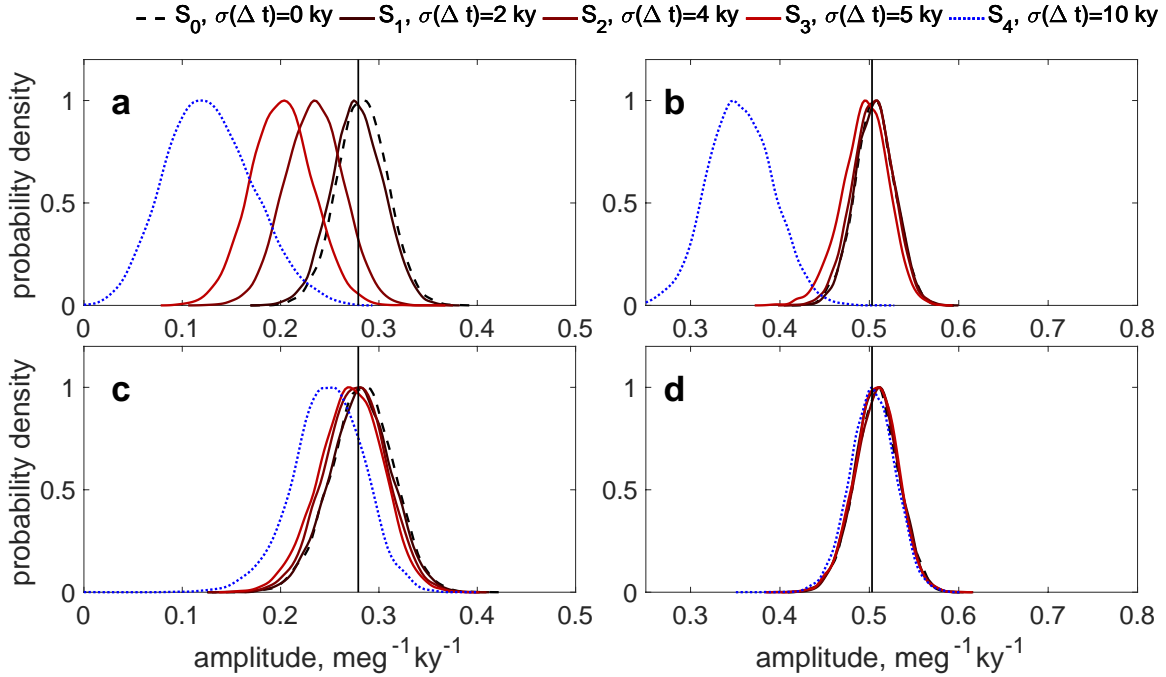


Figure D3: ENOF and spectral estimates of orbital amplitudes in synthetic time-series disrupted with age error. **a** ENOF precession amplitude estimate with age-error standard deviation ranging from 0 ky (dashed black line), to 10 ky (dotted blue line). Each distribution represents 10^4 realizations, and the vertical black line represents the true amplitude. **b** Same as (a), but for obliquity. **c** Same as (a), but where amplitudes are estimated using spectral analysis. **d** Same as (c), but for obliquity.

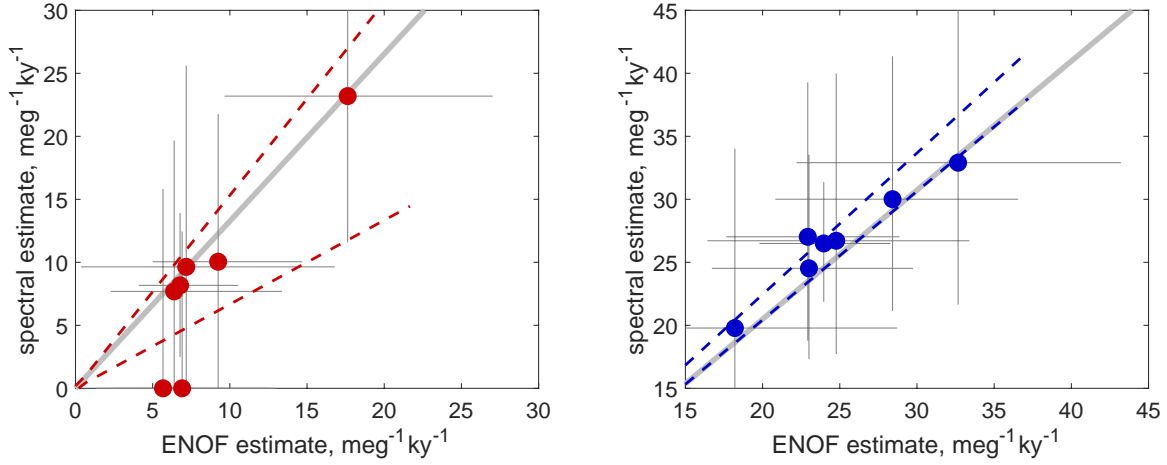


Figure D4: Expected and observed relationship between ENOF and spectral estimates of orbital amplitudes in the presence of age model error. **(a)** Regression of spectral estimates of precession amplitude against ENOF estimates in 10^4 tests on synthetic time-series with SNR=0.5 and with age error having a standard deviation of 5 ky (thick gray line). For comparison, also shown are the ENOF and spectral estimates of precession amplitude in $\delta^{18}\text{O}$ records listed in Table 1 on the depth-derived timescale between 2 and 1 Ma (markers) and their 95% confidence intervals (thin gray bars), as well as the 95% confidence interval for a linear least-squares fit through the markers (dashed lines). Regressions shown here are forced to have zero intercepts. **(b)** same as (a), but for obliquity.

Estimates of orbital amplitudes are not bias-corrected toward higher values to account for age model error, but are bias corrected toward lower values to account for the presence of noise. The overall result is therefore a conservative estimate of orbital amplitude, particularly for precession on account of its being more sensitive to age errors. Although in principle it would be possible to correct estimates for age error, such a correction would inevitably be quite uncertain, and we prefer to make a more conservative test of whether orbital variability is present.

734 *Appendix D.3. Sensitivity to sampling interval*

735 To test the sensitivity of orbital amplitude estimates from both methods to sampling resolution,
736 L2H19 is resampled between 2 and 1 Ma in the depth domain at resolutions ranging from 0.25 ky
737 to 10 ky, then placed on U1308's tuned age model. Sampling resolution in time is determined using
738 Site U1308's average sedimentation rate of 8 cm ky^{-1} (Hodell and Channell, 2016). ENOF and
739 spectral analysis are repeated for each resampled version of the time series. A clear attenuation
740 of the estimated precession amplitude is observed as the sampling interval increases (Figure D5).
741 Precession amplitude estimates are more sensitive to coarsening of sampling resolution than obliquity
742 on account of its shorter period and its being more heavily amplitude- and frequency- modulated.
743 Thus, coarsening leads to a deterioration of the estimated precession-to-obliquity amplitude ratio
744 (Figure D5 b,d). Both methods are similarly sensitive to this problem, with ENOF and spectral
745 analysis respectively giving reductions of 14% and 13% in the ratio when resampling L2H19 at the
746 resolution of DSDP 607.

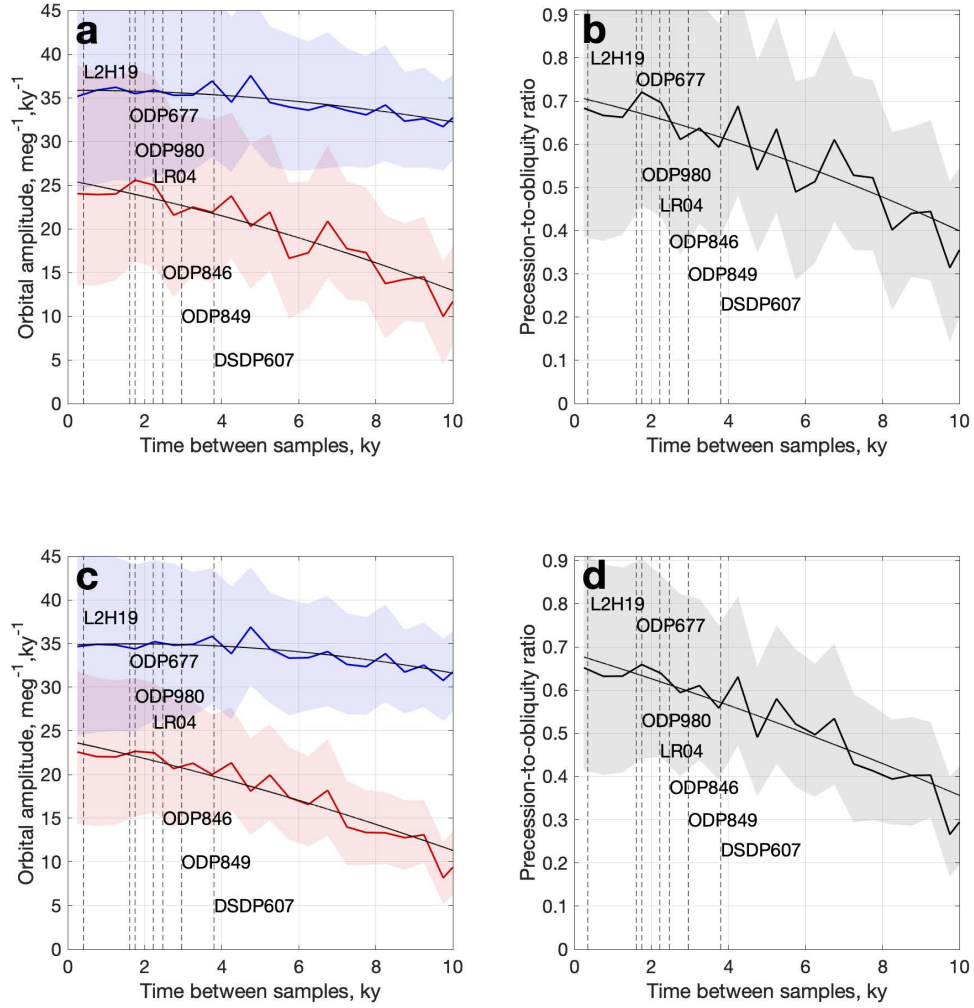


Figure D5: Effect of coarse sampling on the estimation of orbital amplitudes in benthic $\delta^{18}\text{O}$ records. **(a)** Spectral estimates of precession (red) and obliquity (blue) amplitudes and their 95% confidence intervals (red and blue shading) in $d\delta^{18}\text{O}/dt$ between 2 and 1 Ma, using L2H19 on the orbitally-tuned timescale, when L2H19 is resampled in the depth domain at different resolutions. Also indicated are the mean sampling resolution of the records listed in Table 1 over 2-1 Ma (vertical dashed lines). **(b)** The precession-to-obliquity amplitude ratio (black) and its 95% confidence interval (gray shading). **(c)** Same as (a), but using ENOF amplitude estimates. **(d)** Same as (b), but using ENOF amplitude estimates.

747 Appendix E. Phase randomization

748 Phase randomization follows the approach described in Schreiber and Schmitz (2000), which is
 749 repeated here. The phase-randomized (surrogate) time-series, \tilde{s}_n , is given by:

$$\tilde{s}_n = \frac{1}{\sqrt{N}} \sum_{k=0}^{N-1} e^{i\alpha_k} |S_k| e^{-i2\pi kn/N} \quad (\text{E.1})$$

750 where $0 < \alpha_k \leq 2\pi$ are uniform random numbers, S_k are from the discrete Fourier transform,

$$|S_k|^2 = \left| \frac{1}{\sqrt{N}} \sum_{n=0}^{N-1} s_n e^{i2\pi kn/N} \right|^2, \quad (\text{E.2})$$

751 and s_n is the original time series.

752 Appendix F. Ice sheet and energy balance model parameters

Symbol	Value	Unit	Parameter
ρ_i	900	kg m ⁻³	Density of ice
ρ_w	1000	kg m ⁻³	Density of water
ρ_m	3300	kg m ⁻³	Density of mantle
ρ_a	1.5	kg m ⁻³	Density of air
k_i	4	J m ⁻¹ K s	Thermal conductivity of ice
k	0.03	m ² /kg ⁻¹	Mass absorption coefficient, water
g	9.8	ms ⁻²	Gravitational acceleration
σ	5.67×10^{-8}	W m ⁻² K ⁻⁴	Stefan Boltzmann constant
C_d	0.011		Drag coefficient
L_v	2.5×10^6	J kg ⁻¹	Latent heat of vaporization
L_m	3.34×10^5	J kg ⁻¹	Latent heat of melting
L_s	2.84×10^6	J kg ⁻¹	Latent heat of sublimation
a	6.37×10^6	m	Radius of earth
K	273.15	K	Melting temperature of water
C_p	2100	J kg ⁻¹ K ⁻¹	Specific heat capacity, water
C_{air}	1.5	J kg ⁻¹ K ⁻¹	Specific heat capacity, air
C_{ss}	$10 \rho_i C_p$	J m ⁻² K ⁻¹	Heat capacity of subsurface layer
C_s	$5 \rho_i C_p$	J m ⁻² K ⁻¹	Heat capacity of surface
C_a	$5000 \rho_a C_{air}$	J m ⁻² K ⁻¹	Heat capacity of atmosphere
K_s	5	J/K	Sensible heat flux coefficient
H_m	5200	m	Starting thickness of lower atmospheric layer
H_{tm}	2000	m	Thickness of upper atmospheric layer
α_l	0.3	-	Land albedo
α_i	0.8	-	Ice albedo
A	0.2	-	Atmosphere absorption
R	0.3	-	Atmosphere reflection
T	0.5	-	Atmosphere transmission
ϵ_a	0.85	-	Longwave emissivity

P	1	m/a	Precipitation rate
Γ_m	6.35	K/km	Moist adiabatic lapse rate

Table F.3: Energy balance constants and parameters for the model described in section 6.

Symbol	Value	Unit	Parameter
n	3	-	Glen's law exponent
m	1.25	-	Stress-strain law exponent
A_{ice}	7.71×10^{-29}	$\text{Pa}^{-3} \text{ s}^{-1}$	Ice deformability
T_b	5000	years	Bed depression time
H_{eq}	0		Equilibrium surface height
ρ_s	2390	kg m^{-3}	Bulk sediment density
ρ_b	3370	kg m^{-3}	Bedrock density
u_o	3×10^9	$\text{Pa} \cdot \text{s}$	Reference sediment viscosity
h_s	10	m	Thickness of sediment layer
D_o	2.5×10^{-14}	s^{-1}	Reference deformation rate
ϕ_{sed}	22	degrees	Angle of internal friction

Table F.4: Ice sheet and sediment layer parameters for the model described in section 6.

Appendix F.1. Sensitivity tests

Ten model simulations spanning 3 to 1 Ma with no background trend in the climate, but different mean climate states, were conducted to test the effect of the background state on the partitioning of orbital energy in simulated ice volume. Supplemental files include all ten runs, with atmospheric radiation emission levels ranging from 6.5 km to 7.2 km. Three runs are displayed in Figure F1, and demonstrate a stronger expression of precession when the mean temperature is cooler and the ice sheet terminus lies further south.

Note that other mechanisms not accounted for in the EBM may also influence an ice sheet's response to orbital forcing. For example, a more robust treatment of the temperature dependence of precipitation, which the EBM treats as constant, may influence the net mass balance. Some subglacial mechanisms, such as basal melting, are also neglected, as is the possible role of a partial marine

766 margin and associated ice mass loss by calving.

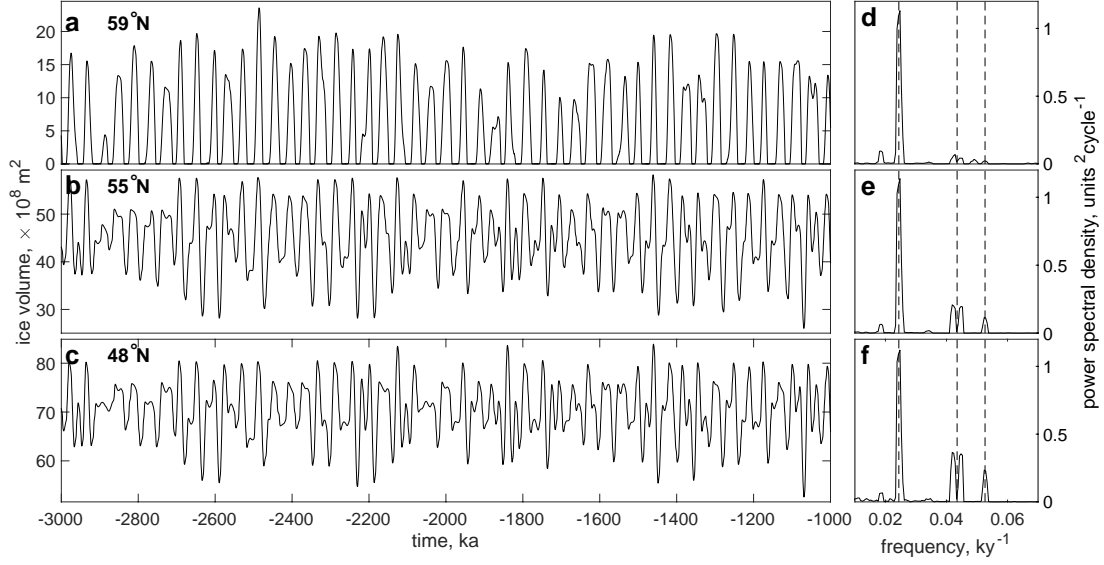


Figure F1: Model ice volume between 3 and 1 Ma under varying background conditions. **(a)** Simulated ice volume when a constant emission level of 7.20 km is used, with other parameters as listed in Table F.4. Bold numbers represent the latitude of the southernmost extent of the ice sheet terminus. **(b-c)** Same as (a), but for emission levels of 6.81 km and 6.50 km. **(d-f)** Power spectral density for the simulated ice volume curves in panels (a)-(c), normalized by the power at $1/41 \text{ ky}^{-1}$, with dashed lines indicating the $1/41$, $1/23$, and $1/19 \text{ ky}^{-1}$ frequencies.

- 767 Adhémar, J. (1842). *Révolutions de la mer*. Carilian-Goeury et V. Dalmont.
- 768 Alley, R. B. (1991). Deforming-bed origin for southern Laurentide till sheets? *Journal of Glaciology*,
769 37(125):67–76.
- 770 Ashkenazy, Y. and Tziperman, E. (2004). Are the 41 kyr glacial oscillations a linear response to
771 Milankovitch forcing? *Quaternary Science Reviews*, 23(18-19):1879–1890.
- 772 Bates, D. and Watts, D. (1988). *Nonlinear regression analysis and its applications*. Wiley.
- 773 Berger, A., Li, X., and Loutre, M.-F. (1999). Modelling northern hemisphere ice volume over the
774 last 3 Ma. *Quaternary Science Reviews*, 18(1):1–11.
- 775 Berger, A. and Loutre, M.-F. (1991). Insolation values for the climate of the last 10 million years.
776 *Quaternary Science Reviews*, 10(4):297–317.
- 777 Bintanja, R. and van de Wal, R. (2008). North American ice-sheet dynamics and the onset of
778 100,000-year glacial cycles. *Nature*, 454(7206):869.
- 779 Bintanja, R., van de Wal, R., and Oerlemans, J. (2005). Modelled atmospheric temperatures and
780 global sea levels over the past million years. *Nature*, 437(7055):125.
- 781 Bolton, C., Wilson, P., Bailey, I., Friedrich, O., Beer, C., Becker, J., Baranwal, S., and Schiebel, R.
782 (2010). Millennial-scale climate variability in the subpolar North Atlantic Ocean during the late
783 Pliocene. *Paleoceanography*, 25(4).
- 784 Bracewell, R. N. (1986). *The Fourier transform and its applications*, volume 31999. McGraw-Hill
785 New York.
- 786 Broecker, W. (1982). Ocean chemistry during glacial time. *Geochimica et Cosmochimica Acta*,
787 46(10):1689–1705.

788 Broecker, W. S., Thurber, D. L., Goddard, J., Ku, T.-L., Matthews, R., and Mesolella, K. J. (1968).
789 Milankovitch hypothesis supported by precise dating of coral reefs and deep-sea sediments. *Science*,
790 159(3812):297–300.

791 Burns, J. A. (1976). Elementary derivation of the perturbation equations of celestial mechanics.
792 *American Journal of Physics*, 44(10):944–949.

793 Caballero-Gill, R., Herbert, T. D., and Dowsett, H. (2019). 100-kyr Paced Climate Change in the
794 Pliocene Warm Period, Southwest Pacific. *Paleoceanography and Paleoclimatology*, 34(4):524–545.

795 Channell, J., Hodell, D., and Curtis, J. (2016). Relative paleointensity (RPI) and oxygen isotope
796 stratigraphy at IODP Site U1308: North Atlantic RPI stack for 1.2–2.2 Ma (NARPI-2200) and
797 age of the Olduvai Subchron. *Quaternary Science Reviews*, 131:1–19.

798 Channell, J., Hodell, D., Xuan, C., Mazaud, A., and Stoner, J. (2008). Age calibrated relative
799 paleointensity for the last 1.5 myr at iodp site u1308 (north atlantic). *Earth and Planetary*
800 *Science Letters*, 274(1-2):59–71.

801 Clark, P. and Pollard, D. (1998). Origin of the middle Pleistocene transition by ice sheet erosion of
802 regolith. *Paleoceanography and Paleoclimatology*, 13(1):1–9.

803 Croll, J. (1864). On the physical cause of the change of climate during geological epochs. *The*
804 *London, Edinburgh, and Dublin Philosophical Magazine and Journal of Science*, 28(187):121–137.

805 Duplessy, J.-C., Moyes, J., and Pujol, C. (1980). Deep water formation in the North Atlantic Ocean
806 during the last ice age. *Nature*, 286(5772):479.

807 Elderfield, H., Ferretti, P., Greaves, M., Crowhurst, S., McCave, I., Hodell, D., and Piotrowski,
808 A. (2012). Evolution of ocean temperature and ice volume through the mid-Pleistocene climate
809 transition. *Science*, 337(6095):704–709.

810 Flower, B. P., Oppo, D. W., McManus, J. F., Venz, K., Hodell, D., and Cullen, J. L. (2000). North
811 Atlantic intermediate to deep water circulation and chemical stratification during the past 1 Myr.
812 *Paleoceanography*, 15(4):388–403.

813 Gildor, H. and Tziperman, E. (2000). Sea ice as the glacial cycles’ climate switch: Role of seasonal
814 and orbital forcing. *Paleoceanography and Paleoclimatology*, 15(6):605–615.

815 Hays, J., Imbrie, J., Shackleton, N., et al. (1976). Variations in the Earth’s orbit: pacemaker of the
816 ice ages. *Science*, 194(4270):1121–1132.

817 Hodell, D. and Channell, J. (2016). Mode transitions in Northern Hemisphere glaciation: co-
818 evolution of millennial and orbital variability in Quaternary climate. *Climate of the Past*,
819 12(9):1805–1828.

820 Huybers, P. (2006). Early Pleistocene glacial cycles and the integrated summer insolation forcing.
821 *Science*, 313(5786):508–511.

822 Huybers, P. (2007). Glacial variability over the last two million years: an extended depth-derived
823 agemodel, continuous obliquity pacing, and the Pleistocene progression. *Quaternary Science Re-*
824 *views*, 26(1-2):37–55.

825 Huybers, P. and Aharonson, O. (2010). Orbital tuning, eccentricity, and the frequency modulation
826 of climatic precession. *Paleoceanography*, 25(4).

827 Huybers, P. and Tziperman, E. (2008). Integrated summer insolation forcing and 40,000-year glacial
828 cycles: The perspective from an ice-sheet/energy-balance model. *Paleoceanography and Paleocli-*
829 *matology*, 23(1).

830 Huybers, P. and Wunsch, C. (2003). Rectification and precession signals in the climate system.
831 *Geophysical Research Letters*, 30(19).

832 Huybers, P. and Wunsch, C. (2004). A depth-derived Pleistocene age model: Uncertainty estimates,
833 sedimentation variability, and nonlinear climate change. *Paleoceanography and Paleoclimatology*,
834 19(1).

835 Imbrie, J., Berger, A., Boyle, E., Clemens, S., Duffy, A., Howard, W., Kukla, G., Kutzbach, J.,
836 Martinson, D., McIntyre, A., et al. (1993). On the structure and origin of major glaciation cycles
837 2. The 100,000-year cycle. *Paleoceanography*, 8(6):699–735.

838 Imbrie, J., Boyle, E., Clemens, S., Duffy, A., Howard, W., Kukla, G., Kutzbach, J., Martinson, D.,
839 McIntyre, A., Mix, A., et al. (1992). On the structure and origin of major glaciation cycles 1.
840 Linear responses to Milankovitch forcing. *Paleoceanography*, 7(6):701–738.

841 Imbrie, J. and Imbrie, J. (1980). Modeling the climatic response to orbital variations. *Science*,
842 207(4434):943–953.

843 Kawamura, K., Parrenin, F., Lisiecki, L., Uemura, R., Vimeux, F., Severinghaus, J. P., Hutterli,
844 M. A., Nakazawa, T., Aoki, S., Jouzel, J., et al. (2007). Northern Hemisphere forcing of climatic
845 cycles in Antarctica over the past 360,000 years. *Nature*, 448(7156):912.

846 Lawrence, K., Sostdian, S., White, H., and Rosenthal, Y. (2010). North Atlantic climate evolution
847 through the Plio-Pleistocene climate transitions. *Earth and Planetary Science Letters*, 300(3-
848 4):329–342.

849 Lisiecki, L. (2010). Links between eccentricity forcing and the 100,000-year glacial cycle. *Nature*
850 *Geoscience*, 3(5):349.

851 Lisiecki, L. and Raymo, M. (2005). A Pliocene-Pleistocene stack of 57 globally distributed benthic
852 $\delta^{18}\text{O}$ records. *Paleoceanography*, 20(1).

853 Lisiecki, L. E. and Raymo, M. E. (2007). Plio–Pleistocene climate evolution: trends and transitions
854 in glacial cycle dynamics. *Quaternary Science Reviews*, 26(1-2):56–69.

- 855 Loutre, M.-F., Paillard, D., Vimeux, F., and Cortijo, E. (2004). Does mean annual insolation have
856 the potential to change the climate? *Earth and Planetary Science Letters*, 221(1-4):1–14.
- 857 Mc Intyre, K., Ravelo, A., and Delaney, M. (1999). North Atlantic intermediate waters in the late
858 Pliocene to early Pleistocene. *Paleoceanography*, 14(3):324–335.
- 859 McManus, J. F., Oppo, D. W., and Cullen, J. L. (1999). A 0.5-million-year record of millennial-scale
860 climate variability in the North Atlantic. *Science*, 283(5404):971–975.
- 861 Milankovitch, M. (1941). Kanon der Erdbestrahlung und seine Anwendung auf das Eiszeitenproblem.
862 *Royal Serbian Academy Special Publication*, 133:1–633.
- 863 Mix, A. C., Le, J., and Shackleton, N. (1995a). Benthic foraminiferal stable isotope stratigraphy of
864 Site 846: 0-1.8 Ma. In *Proceedings of the Ocean Drilling Program. Scientific Results*, volume 138.
- 865 Mix, A. C., Pisias, N. G., Rugh, W., Wilson, J., Morey, A., and Hagelberg, T. (1995b). Benthic
866 foraminifer stable isotope record from Site 849 (0-5 Ma): Local and global climate changes.
- 867 Murphy, J. J. (1869). On the nature and cause of the glacial climate. *Quarterly Journal of the*
868 *Geological Society*, 25(1-2):350–356.
- 869 Nisancioglu, K. (2004). *Modeling the impact of atmospheric moisture transport on global ice volume*.
870 PhD thesis, Massachusetts Institute of Technology.
- 871 Obrochta, S., Crowley, T., Channell, J., Hodell, D., Baker, P., Seki, A., and Yokoyama, Y. (2014).
872 Climate variability and ice-sheet dynamics during the last three glaciations. *Earth and Planetary*
873 *Science Letters*, 406:198–212.
- 874 Oppo, D., McManus, J., and Cullen, J. (1998). Abrupt climate events 500,000 to 340,000 years ago:
875 Evidence from subpolar North Atlantic sediments. *Science*, 279(5355):1335–1338.
- 876 Percival, D. and Walden, A. (1993). *Spectral analysis for physical applications*. Cambridge University
877 Press.

878 Pias, N. and Mix, A. (1988). Aliasing of the geologic record and the search for long-period Mi-
879 lankovitch cycles. *Paleoceanography and Paleoclimatology*, 3(5):613–619.

880 Proistosescu, C., Huybers, P., and Maloof, A. C. (2012). To tune or not to tune: Detecting orbital
881 variability in Oligo-Miocene climate records. *Earth and Planetary Science Letters*, 325:100–107.

882 Raymo, M., Lisiecki, L., and Nisancioglu, K. (2006). Plio-Pleistocene ice volume, Antarctic climate,
883 and the global $\delta^{18}\text{O}$ record. *Science*, 313(5786):492–495.

884 Raymo, M. and Nisancioglu, K. (2003). The 41 kyr world: Milankovitch’s other unsolved mystery.
885 *Paleoceanography*, 18(1).

886 Raymo, M. E., Oppo, D. W., Flower, B. P., Hodell, D. A., McManus, J. F., Venz, K., Kleiven, K.,
887 and McIntyre, K. (2004). Stability of North Atlantic water masses in face of pronounced climate
888 variability during the Pleistocene. *Paleoceanography*, 19(2).

889 Roe, G. (2006). In defense of Milankovitch. *Geophysical Research Letters*, 33(24).

890 Rubincam, D. (1994). Insolation in terms of Earth’s orbital parameters. *Theoretical and Applied*
891 *Climatology*, 48(4):195–202.

892 Rubincam, D. (2004). Black body temperature, orbital elements, the Milankovitch precession index,
893 and the Seversmith psychroterms. *Theoretical and Applied Climatology*, 79(1-2):111–131.

894 Ruddiman, W., Raymo, M., Martinson, D., Clement, B., and Backman, J. (1989). Pleistocene
895 evolution: northern hemisphere ice sheets and North Atlantic Ocean. *Paleoceanography and Pa-*
896 *leoclimatology*, 4(4):353–412.

897 Ruddiman, W. F., Raymo, M., and McIntyre, A. (1986). Matuyama 41,000-year cycles: North
898 Atlantic Ocean and Northern Hemisphere ice sheets. *Earth and Planetary Science Letters*, 80(1-
899 2):117–129.

- 900 Schreiber, T. and Schmitz, A. (2000). Surrogate time series. *Physica D: Nonlinear Phenomena*,
901 142(3-4):346–382.
- 902 Shackleton, N., Berger, A., and Peltier, W. (1990). An alternative astronomical calibration of the
903 lower Pleistocene timescale based on ODP Site 677. *Earth and environmental science transactions*
904 *of the royal society of Edinburgh*, 81(4):251–261.
- 905 Tabor, C., Poulsen, C., and Pollard, D. (2015). How obliquity cycles powered early Pleistocene
906 global ice-volume variability. *Geophysical Research Letters*, 42(6):1871–1879.
- 907 Waelbroeck, C., Labeyrie, L., Michel, E., Duplessy, J., McManus, J., Lambeck, K., Balbon, E.,
908 and Labracherie, M. (2002). Sea-level and deep water temperature changes derived from benthic
909 foraminifera isotopic records. *Quaternary Science Reviews*, 21(1-3):295–305.
- 910 Weertman, J. (1964). Rate of growth or shrinkage of nonequilibrium ice sheets. *Journal of Glaciology*,
911 5(38):145–158.
- 912 Wunsch, C. (2003). The spectral description of climate change including the 100 ky energy. *Climate*
913 *Dynamics*, 20(4):353–363.
- 914 Zeeden, C., Meyers, S. R., Lourens, L. J., and Hilgen, F. J. (2015). Testing astronomically tuned
915 age models. *Paleoceanography*, 30(4):369–383.